Open-loop control of cavity oscillations with harmonic forcings

Denis Sipp

Journal of Fluid Mechanics / Volume 708 / October 2012, pp 439 - 468
DOI: 10.1017/jfm.2012.329, Published online: 12 September 2012

J. Fluid Mech. (2012), *vol.* 708, *pp.* 439–468.
doi:10.1017/jfm.2012.329

Open-loop control of cavity oscillations with harmonic forcings

Denis Sipp†

ONERA DAFE-The French Aerospace Lab, 8 rue des Vertugardins, 92190 Meudon, France

(Received 8 February 2012; revised 22 May 2012; accepted 25 June 2012)

This article deals with open-loop control of open-cavity flows with harmonic forcings. Two-dimensional laminar open-cavity flows usually undergo a supercritical Hopf bifurcation at some critical Reynolds number: a global mode becomes unstable and its amplitude converges towards a limit cycle. Such behaviour may be accurately captured by a Stuart–Landau equation, which governs the amplitude of the global mode. In the present article, we study the effect on such a flow of a forcing characterized by its frequency ω_f, its amplitude E' and its spatial structure $\boldsymbol{f}_E$. The system reacts like a forced Van der Pol oscillator. In the general case, such a forcing modifies the linear dynamics of the global mode. It is then possible to predict preferred forcing frequencies ω_f, at which the global mode may be stabilized with the smallest possible forcing amplitude E'. In the case of a forcing frequency close to the frequency of the global mode, a locking phenomenon may be observed if the forcing amplitude E' is sufficiently high: the frequency of the flow on the limit cycle may be modified with a very small forcing amplitude E'. In each case, we compute all harmonics of the flow field and all coefficients that enter the amplitude equations. In particular, it is possible to find preferred forcing structures $\boldsymbol{f}_E$ that achieve strongest impact on the flow field. In the general case, these are the optimal forcings, which are defined as the forcings that trigger the strongest energy response. In the case of a forcing frequency close to the frequency of the global mode, a forcing structure equal to the adjoint global mode ensures the lowest forcing amplitude E'. All predictions given by the amplitude equations are checked against direct numerical simulations conducted at a supercritical Reynolds number. We show that a global mode may effectively be stabilized by a high-frequency harmonic forcing, which achieves suppression of the perturbation frequencies that are lower than the forcing frequency, and that a near-resonant forcing achieves locking of the flow onto the forcing frequency, as predicted by the amplitude equations.

Key words: instability control, low-dimensional models, separated flows

1. Introduction

Open-loop control of flows behaving like oscillators is an important issue in fluid mechanics. Oscillators are flows displaying unsteadiness characterized by a well-defined frequency, which is rather insensitive to low-level external noise (Huerre & Rossi 1998). Bluff bodies such as cylinders or open cavities are examples of oscillators. The unsteady behaviour associated with the vortex shedding phenomenon

† Email address for correspondence: denis.sipp@onera.fr

behind a cylinder is responsible for serious structural vibrations and significant increased drag. Choi, Jeon & Kim (2008) have made an extensive review of flow-control over bluff bodies. Here we focus on open-loop control strategies that directly modify the properties of the wake (and not the boundary layer). The control objective consists in either suppressing the natural frequency of the flow, or, if this is not possible, shifting this frequency. The second objective is less ambitious but may be justified in a fluid-induced vibration problem: the only dangerous flow instabilities are those where the fluid's frequencies match those of the structural modes. Hence, shifting the flow's dangerous frequencies a little may be sufficient to solve the problem.

Choi *et al.* (2008) mention both steady (blowing and suction, modification of the geometry) and time-periodic control means (blowing and suction, synthetic jets) of attenuating vortex shedding. Also, for cylinder flow, Strykowski & Sreenivasan (1990) managed to suppress the vortex shedding phenomenon by introducing a small control cylinder in the flow: by the action and reaction principle, the control cylinder exerts a steady forcing on the flow field. Amitay *et al.* (1998) and Glezer & Amitay (2002) showed how high-frequency forcing with synthetic jets allowed a significant modification in the mean properties of the flow field. The strong periodic fluctuations over an open cavity (Rossiter 1962) may be suppressed by introducing a rod near the leading edge of the cavity (Illy, Geffroy & Jacquin 2008). Stanek *et al.* (2007) argued that this phenomenon was due to the high-frequency forcing triggered by the vortex shedding behind the small rod which generated perturbations that rendered the mean flow stable. Keirsbulck *et al.* (2008), on the other hand, argues that it is the steady part of the forcing related to the mean drag of the control cylinder which is responsible for the stabilization.

The behaviour of oscillator flows may be described by a local stability approach when the flow field is weakly non-parallel. Oscillator flows correspond to absolutely unstable flows (Huerre & Rossi 1998). In the case of steady forcing, Hwang & Choi (2006) analysed how the extent of the absolutely unstable region may be reduced by base flow modifications. In the case of harmonic forcing, Pier (2003) showed how an upstream-located harmonic forcing allows the tuning of the entire system to any frequency in a wide range.

In a global approach, solving for the streamwise direction, oscillators are characterized by a Jacobian which displays an unstable eigenvalue (Sipp *et al.* 2010). For example, in the case of the cylinder flow, Jackson (1987) was the first to show that an eigenvalue characterized by a non-zero frequency became unstable for $Re > 47$. The associated structure – the so-called global mode – will then grow exponentially and, since the bifurcation is supercritical (Provansal, Mathis & Boyer 1987), the amplitude of the global mode will saturate and the flow will converge on a limit cycle. For slightly supercritical Reynolds numbers, Sipp & Lebedev (2007) showed that the amplitude of the global mode was governed by a Stuart–Landau equation, whose coefficients may be computed from the interaction of various components of the flow field (including the base flow, the global mode, the zeroth harmonic, the second harmonic, etc.) Since then, other oscillator flows have been described in the global approach by amplitude equations: the open-cavity flow (Sipp & Lebedev 2007), the flow behind an axisymmetric disc (Meliga, Chomaz & Sipp 2009), or the flow around a spring-mounted cylinder (Meliga & Chomaz 2011). A first theoretical approach to open-loop control of oscillator flows was introduced by Hill (1992), Chomaz (2005), Giannetti & Luchini (2007), Marquet *et al.* (2008*a*) and Meliga, Sipp & Chomaz (2010). These authors considered a steady forcing acting on the base flow (or also a steady suction or blowing at a wall), which aims at stabilizing the unstable global

mode. Giannetti, Camarri & Luchini (2010) have extended these approaches to the case of time-periodic base flows to study of the sensitivity of limit cycles. All these works are based on adjoint methods to define sensitivity maps showing regions in the flow where the eigenvalue of the global mode is particularly sensitive to the introduction of forcing. Results compare favourably with the experimental results of Strykowski & Sreenivasan (1990), who introduced a small control cylinder in the wake of a cylinder to suppress the von Kármán vortex shedding. In these papers, the size of the control cylinder was chosen sufficiently small to ensure that there was no vortex shedding behind the small control cylinder. Hence, the force that the flow exerts on the small control cylinder is steady, and by the action and reaction principle, the force exerted by the small control cylinder on the flow field is also steady. This is compatible with the sensitivity theory, which only accounts for a steady forcing acting on the flow field.

Now, if the size of the small control cylinder is sufficiently high, then vortex shedding will occur behind the small control cylinder, and the force exerted by the small control cylinder on the flow field will be unsteady and periodic with a frequency characterized by a Strouhal number of about ~ 0.2 (the Strouhal number being based on the diameter of the control cylinder and on the local velocity field of the flow near the control cylinder). What is the effect of this harmonic forcing on the dynamics of the unstable global mode? Can we stabilize the flow using this unsteady forcing? If not, can we change the frequency of the flow? In the present article, we will try to answer these questions by extending the nonlinear Stuart–Landau equation governing the amplitude of the global mode to take into account the effect of a harmonic forcing characterized by an arbitrary frequency and arbitrary spatial shape.

The present study will be guided by the results on the forced Van der Pol oscillator (Bender & Orszag 1978; Fauve 1998). Indeed, such a model problem mimics qualitatively well a flow field undergoing a supercritical Hopf bifurcation and subject to a harmonic forcing. Hence, we will retrieve interesting features such as the locking phenomenon that arises when the forcing frequency is close to the natural frequency of the flow field.

The issue of mean flow stability will also be particularly discussed. The mean flow is not an equilibrium point of the Navier–Stokes equations. It corresponds to the time-average of the unsteady flow. Therefore, the relevance of a stability analysis applied to a mean flow is questionable. Sipp & Lebedev (2007) showed that in certain circumstances the mean flow exhibits a global mode with zero amplification rate and a frequency which matches the frequency of the true flow on the limit cycle. These conditions hold almost perfectly for the cylinder flow near the first bifurcation at $Re = 47$, while they nearly hold for the open-cavity flow. Barkley (2006) even showed that such a behaviour may be observed far beyond the bifurcation threshold, for Reynolds numbers up to $Re = 180$ in the case of the cylinder flow. The question that we will try to answer in this paper is the following. In the case of open-loop control, if we manage to stabilize the global mode, is the resulting mean flow still marginally stable? If we only manage to shift the frequency of the flow on the limit cycle, does the mean flow reflect the frequency of the true flow on the limit cycle?

As for the configuration, rather than the cylinder flow, we will choose the laminar two-dimensional open-cavity flow, which undergoes a supercritical Hopf bifurcation at a given Reynolds number. This flow was chosen since the linear frequency response of the flow is much richer (see below) than that obtained with a cylinder. We will see in particular that there exist preferred frequencies and locations of the harmonic forcing to efficiently manipulate the flow.

The article is organized as follows. First, in § 2, we will present the configuration and recall that the dynamics is governed by a Stuart–Landau amplitude equation. Then in § 3 we will study the non-resonant forcing case, where the forcing frequency does not match the natural frequency of the flow. In particular, we will add a term in the amplitude equation to take into account the forcing (§ 3.1). We will analyse the various control strategies (§ 3.2), show that for each frequency there exist preferred forcing structures (§ 3.3) and compare the theoretical results to those of direct numerical simulation conducted at a supercritical Reynolds number (§ 3.4). The limitations of the present asymptotic approach will be discussed in § 3.5 and the stability of the resulting mean flows will be discussed in § 3.6. Then in (§ 4 we will analyse the case of steady (zero-frequency) forcing and the case of resonant forcing, where the forcing frequency is close to the natural frequency of the flow. In the latter case, results will briefly be compared to direct numerical simulations. Finally, in § 5, we will conclude and mention some prospects for the future.

2. Configuration, eigenvalues, limit-cycle

We consider an incompressible homogeneous flow over an open cavity, similar to the one studied in Sipp & Lebedev (2007). The cavity is square, the origin of the Cartesian coordinate system being located at the leading-edge corner of the cavity. In the following, we use the free-stream velocity and the cavity length to make all quantities non-dimensional. We use the streamwise u, cross-stream v components of the velocity and the pressure p to describe the flow. The flow is uniform ($u = 1, v = 0$) at the inlet ($x = -2.4, 0 \leqslant y \leqslant 0.5$) and a slip-boundary condition ($\partial_y u = 0, v = 0$) is imposed on the upper boundary ($-2.4 \leqslant x \leqslant 2.5, y = 0.5$) and on the upstream part of the lower boundary ($-2.4 \leqslant x \leqslant -1.6, y = 0$). On the remaining part of the lower boundary $x \geqslant -1.6$, we use a no-slip boundary condition ($u = 0, v = 0$). This partitioning of the lower boundary enables us to vary the boundary layer thickness at the leading edge of the cavity. At the outlet ($x = 2.5, 0 \leqslant y \leqslant 0.5$), a standard free-stream boundary condition is applied: $-p\boldsymbol{n} + \boldsymbol{\nabla u} \cdot \boldsymbol{n} = 0$.

The Reynolds number will be chosen close to $Re_c = 5396$, this specific value corresponding to the threshold of instability (see below). In the following, we will use parameter δ' to specify the actual Reynolds number: $Re^{-1} = Re_c^{-1} - \delta'$. The governing equations then read

$$\partial_t \boldsymbol{u} + \boldsymbol{\nabla u} \cdot \boldsymbol{u} = -\boldsymbol{\nabla} p + (Re_c^{-1} - \delta')\boldsymbol{\Delta u}, \quad \boldsymbol{\nabla} \cdot \boldsymbol{u} = \boldsymbol{0}. \tag{2.1}$$

We focus on the case where the Reynolds number is close to criticality: $\delta' = \epsilon\delta$ with $\epsilon \ll 1$. We may look for a solution of the flow field $\boldsymbol{q} = (u, v, p)^{\mathrm{T}}$ in the form

$$\boldsymbol{q} = \boldsymbol{q}_0 + \epsilon^{1/2}[A\mathrm{e}^{\mathrm{i}\omega_c t}\boldsymbol{q}_A + \mathrm{c.c.}] + \epsilon[\delta\boldsymbol{q}_\delta + |A|^2\boldsymbol{q}_{A\bar{A}} + (A^2\mathrm{e}^{2\mathrm{i}\omega_c t}\boldsymbol{q}_{AA} + \mathrm{c.c.})]. \tag{2.2}$$

If this development is introduced in the governing equations (2.1), a series of equations is obtained at various orders in ϵ:

$$\boldsymbol{\nabla u}_0 \cdot \boldsymbol{u}_0 = -\boldsymbol{\nabla} p_0 + Re_c^{-1}\boldsymbol{\Delta u}_0, \quad \boldsymbol{\nabla} \cdot \boldsymbol{u}_0 = \boldsymbol{0}, \tag{2.3}$$

$$(\mathrm{i}\omega_c \mathscr{P}\mathscr{P}^{\mathrm{T}} + \mathscr{M})\boldsymbol{q}_A = \boldsymbol{0}, \tag{2.4}$$

$$\mathscr{M}\boldsymbol{q}_\delta = -\mathscr{P}(\boldsymbol{\Delta u}_0), \tag{2.5}$$

$$\mathscr{M}\boldsymbol{q}_{A\bar{A}} = -\mathscr{P}(\boldsymbol{\nabla u}_A \cdot \overline{\boldsymbol{u}_A} + \overline{\boldsymbol{\nabla u}_A} \cdot \boldsymbol{u}_A), \tag{2.6}$$

$$(2\mathrm{i}\omega_c \mathscr{P}\mathscr{P}^{\mathrm{T}} + \mathscr{M})\boldsymbol{q}_{AA} = -\mathscr{P}(\boldsymbol{\nabla u}_A \cdot \boldsymbol{u}_A). \tag{2.7}$$

Equations (2.3), (2.4) and (2.5)–(2.7) are respectively obtained at order ϵ^0, $\epsilon^{1/2}$ and ϵ.

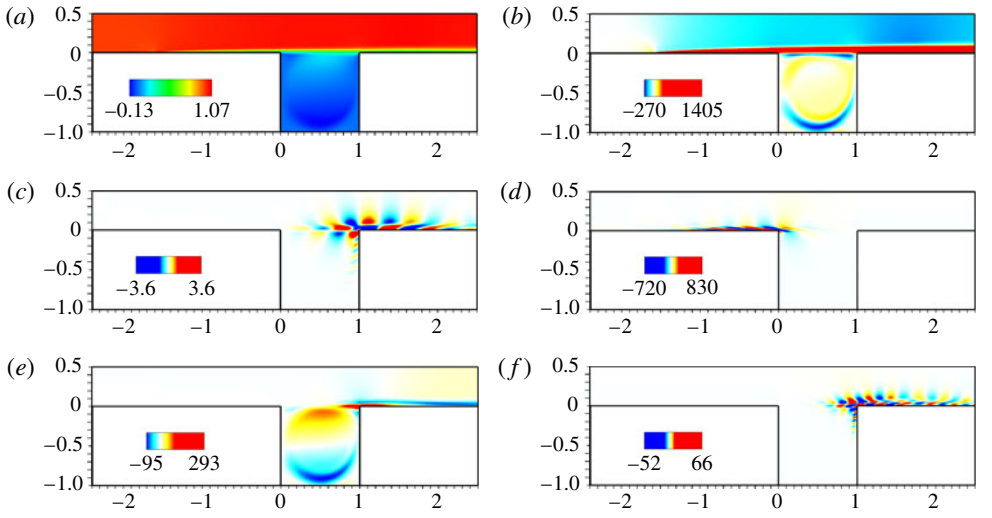

FIGURE 1. $Re = 5396$. Streamwise component of various flows involved in expansion (2.2): (*a*) base flow u_0; (*b*) base flow modification due to increase of Reynolds number u_δ; (*c*) marginal global mode or first harmonic $\mathrm{Re}(u_A)$; (*d*) marginal adjoint global mode $\mathrm{Re}(\tilde{u}_A)$; (*e*) zeroth harmonic $u_{A\bar{A}}$; (*f*) second harmonic $\mathrm{Re}(u_{AA})$.

Equation (2.3) together with the boundary conditions mentioned above defines a base flow, which is an equilibrium point of the Navier–Stokes equations (2.1). This nonlinear equation may be solved thanks to a Newton method. We use the same techniques and spatial discretizations as those presented in Sipp & Lebedev (2007): the unknowns (u, v, p) are spatially discretized on an unstructured mesh using finite elements (here P2–P1 Taylor–Hood elements), the resulting matrices being generated by the FreeFem++ software (http://www.freefem.org) and inverted thanks to a direct-LU solver Amestoy *et al.* (2001). The mesh comprises 259 050 triangles, which yields 1171 098 degrees of freedom in a (u, v, p) quantity. The size of the triangles h is equal to $h = 1/350$ in the boundary layers and in the shear layer. The mesh becomes progressively coarser in the free stream where $h = 1/100$ and inside the cavity where $h = 1/50$. The base flow at $Re = 5396$ is shown in figure 1(*a*) with iso-values of the streamwise velocity. We clearly observe a boundary layer which starts developing at $x = -1.6$, a thin shear layer on top of the cavity and a recirculation region inside the cavity.

Equations (2.4)–(2.7) together with the homogeneous versions of the boundary conditions respectively define the marginal global mode, the base flow modification due to the increase of the Reynolds number δ', the zeroth and second harmonics. These equations involve the following linear operators:

$$\mathscr{M} = \begin{pmatrix} \boldsymbol{\nabla} \boldsymbol{u}_0 \cdot () + \boldsymbol{\nabla}() \cdot \boldsymbol{u}_0 - Re_c^{-1} \Delta & \boldsymbol{\nabla} \\ \boldsymbol{\nabla} \cdot () & 0 \end{pmatrix}, \quad \mathscr{P} = \begin{pmatrix} \mathscr{I} \\ 0 \end{pmatrix}. \tag{2.8}$$

Here $\mathscr{M}$ is the linearized (around the base flow $\boldsymbol{u}_0$) Navier–Stokes operator, $\mathscr{P}$ a prolongation operator which transforms a $(u, v)^{\mathrm{T}}$ quantity into $(u, v, 0)^{\mathrm{T}}$. Note also that, $^{\mathrm{T}}$ being the transpose, $\mathscr{P}^{\mathrm{T}}$ designates the restriction operator that transforms $(u, v, p)^{\mathrm{T}}$ into $(u, v)^{\mathrm{T}}$.

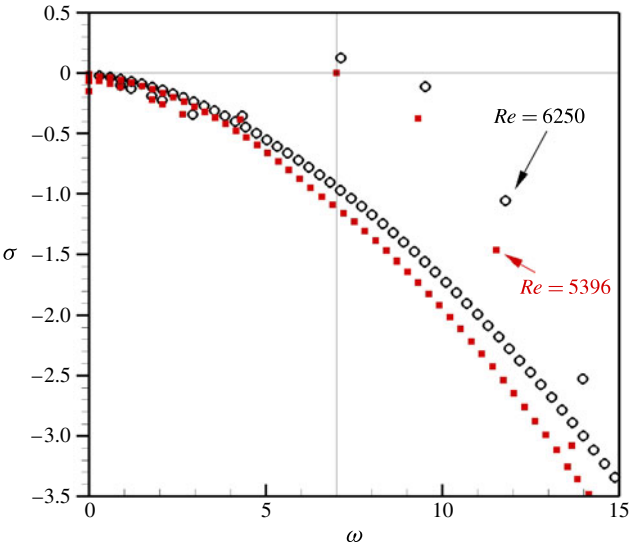

FIGURE 2. (Colour online) Least stable eigenvalues of Jacobian matrix for $Re = 5396$ (squares) and for $Re = 6250$ (open symbols). At the critical Reynolds number $Re = 5396$, there is one marginal global mode characterized by $\omega_c = 7.0$. For the supercritical Reynolds number $Re = 6250$, this global mode becomes unstable.

Equation (2.4) is an eigenproblem with eigenvalue $\lambda = \mathrm{i}\omega_c$ and eigenvector $\boldsymbol{q}_A$. Following Sipp & Lebedev (2007), such a problem may be solved thanks to a Krylov subspace method associated with a shift-and-invert technique (http://www.caam.rice.edu/software/ARPACK/, Lehoucq & Sorensen (1996)). The least stable eigenvalues for $Re = 5396$ and $Re = 6250$ are represented in figure 2 in the (ω, σ) plane, where ω and σ respectively refer to the frequency and the amplification rate. We observe that at $Re = 5396$ there exists one marginal global mode satisfying $(\sigma_c = 0, \omega_c = 7.0)$. For a slightly larger Reynolds number $Re = 6250$, this global mode becomes unstable while all other global modes remain stable. In the following, $\boldsymbol{q}_A$ will refer to the marginal global obtained at criticality $Re = Re_c = 5396$. The streamwise component of the velocity field of this global mode is represented in figure 1(*c*). This mode is seen to take advantage of the Kelvin–Helmholtz instability that develops on the shear layer. Note that the global mode verifies the following arbitrary condition: $v_A(x = 0.75, y = 0) = -0.52052 - 1.57966\mathrm{i}$. This sets the amplitude and phase of the global mode.

Equations (2.5)–(2.7) are non-degenerate linear systems (from figure 2, it is seen that at $Re = 5396$ there are no eigenvalues at $(\sigma = 0, \omega = 0)$ and $(\sigma = 0, \omega = 2\omega_c)$), that may be straightforwardly inverted. The base flow modifications related to the increase of Reynolds number $\boldsymbol{q}_\delta$, the zeroth harmonic $\boldsymbol{q}_{A\bar{A}}$ and the real part of the second harmonic $\boldsymbol{q}_{AA}$ are shown in figure 1(*b*,*e*,*f*) with iso-values of the streamwise velocity. The zero harmonic results from the nonlinear interaction between the global mode $\boldsymbol{q}_A$ with its conjugate $\overline{\boldsymbol{q}_A}$, while the second harmonic stems from the interaction between the global mode $\boldsymbol{q}_A$ with himself. The spatial structures of the various flows reflect their frequency: large-scale structures for the base flow modification and the zeroth harmonic, small-scale features for the second harmonic, which beats at frequency $2\omega_c = 14.0$.

At order $\epsilon^{3/2}$, we obtain forced degenerate linear systems. If we let the amplitude A evolve on a slow time scale $T = \epsilon t$, by enforcing compatibility conditions, we obtain the following equation governing the complex amplitude A of the global mode:

$$\frac{\mathrm{d}A}{\mathrm{d}T} = \eta \delta A - \nu A \left|A\right|^2 . \tag{2.9}$$

Introducing the full amplitude $A' = \epsilon^{1/2} A$ of the global mode and coming back to the unscaled variables $\delta' = \epsilon \delta$ and $t = \epsilon^{-1} T$, one straightforwardly obtains

$$\frac{\mathrm{d}A'}{\mathrm{d}t} = \eta \delta' A' - \nu A' \left|A'\right|^2 . \tag{2.10}$$

The complex constants η and ν are given by

$$\eta = -\langle \tilde{\boldsymbol{u}}_A, \boldsymbol{\nabla} \boldsymbol{u}_A \cdot \boldsymbol{u}_\delta + \boldsymbol{\nabla} \boldsymbol{u}_\delta \cdot \boldsymbol{u}_A + \boldsymbol{\Delta} \boldsymbol{u}_A \rangle, \tag{2.11}$$

$$\nu = \underbrace{\langle \tilde{\boldsymbol{u}}_A, \boldsymbol{\nabla} \boldsymbol{u}_A \cdot \boldsymbol{u}_{A\bar{A}} + \boldsymbol{\nabla} \boldsymbol{u}_{A\bar{A}} \cdot \boldsymbol{u}_A \rangle}_{\nu_{A\bar{A}}} + \underbrace{\langle \tilde{\boldsymbol{u}}_A, \overline{\boldsymbol{\nabla} \boldsymbol{u}_A} \cdot \boldsymbol{u}_{AA} + \boldsymbol{\nabla} \boldsymbol{u}_{AA} \cdot \overline{\boldsymbol{u}_A} \rangle}_{\nu_{AA}}, \tag{2.12}$$

where $\langle \cdot, \cdot \rangle$ designates an energy-based Hermitian scalar product and $\tilde{\boldsymbol{u}}_A$ is the adjoint global mode associated with $\boldsymbol{u}_A$. The adjoint global mode $\tilde{\boldsymbol{q}}_A = (\tilde{u}_A, \tilde{v}_A, \tilde{p}_A)^{\mathrm{T}}$ corresponds to the eigenvector related to the following eigenproblem:

$$(-\mathrm{i}\omega_c \mathscr{P} \mathscr{P}^{\mathrm{T}} + \tilde{\mathscr{M}}) \tilde{\boldsymbol{q}}_A = \boldsymbol{0}, \tag{2.13}$$

$$\tilde{\mathscr{M}} = \begin{pmatrix} (\boldsymbol{\nabla} \boldsymbol{u}_0)^{\mathrm{T}} \cdot () - \boldsymbol{\nabla}() \cdot \boldsymbol{u}_0 - Re_c^{-1} \Delta & -\boldsymbol{\nabla} \\ -\boldsymbol{\nabla} \cdot () & 0 \end{pmatrix}, \tag{2.14}$$

with the normalization condition $\langle \tilde{\boldsymbol{u}}_A, \boldsymbol{u}_A \rangle = 1$. The streamwise velocity component of the adjoint global mode is represented in figure 1(*d*). We observe that it is located upstream, near the leading edge of the cavity.

It is also seen that the constant ν is made of two distinct contributions: $\nu_{A\bar{A}}$ relates to the contribution of the zeroth harmonic $\boldsymbol{u}_{A\bar{A}}$ while ν_{AA} relates to that of the second harmonic $\boldsymbol{u}_{AA}$. Numerically, we obtain $\eta = 4688.43 + 4701.23\mathrm{i}$ and $\nu = 390.27 - 142.91\mathrm{i}$. We verify that $\eta_r > 0$, which shows that the flow becomes unstable for $Re > Re_c$, and that $\nu_r > 0$, indicating that the bifurcation is supercritical. On the limit cycle, the oscillation amplitude and frequency of the flow field is given by (Sipp & Lebedev 2007)

$$\left|A'\right|^{LC} = \sqrt{\frac{\eta_r}{\nu_r} \delta'}, \tag{2.15}$$

$$\omega^{LC} = \omega_c + \eta_i \delta' - \frac{\eta_r}{\nu_r} \nu_i \delta'. \tag{2.16}$$

The first, second and third terms on the right-hand side of (2.16), respectively, correspond to the frequency of the marginal global mode, the shift in frequency of the global mode associated to the increase in Reynolds number δ' and the shift in frequency associated to nonlinear interactions linked to the zeroth and second harmonics.

In the following, we aim at suppressing the fluctuations at the frequency ω^{LC}. As mentioned in § 1, two strategies can be followed. The most ambitious one consists in stabilizing the unstable global mode, which suppresses all fluctuations linked to the global mode. The second one only aims at shifting the frequency of the global mode on the limit cycle ω^{LC}. Having done this, the global mode is still unstable and the flow

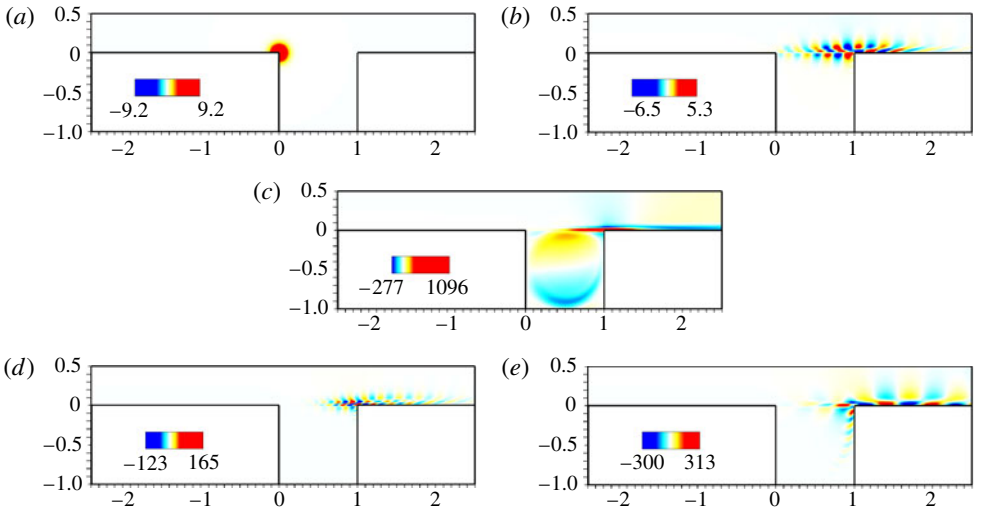

FIGURE 3. $Re = 5396$. Various flows related to fixed harmonic forcing at $\omega_f = 13$ and involved in expansion (3.3). (*a*) Cross-stream component of forcing g_E; (*b*) streamwise component of forcing response $\mathrm{Re}(u_E)$; (*c*) streamwise component of zeroth harmonic $u_{E\bar{E}}$; (*d*) streamwise component of $(\omega_c + \omega_f)$-harmonic $\mathrm{Re}(u_{AE})$; (*e*) streamwise component of $(\omega_c - \omega_f)$-harmonic $\mathrm{Re}(u_{A\bar{E}})$.

field still oscillates on a limit cycle but at a different frequency, which is hopefully less dangerous for the system.

3. Control by harmonic forcing in the non-resonant case

We will now consider a given harmonic forcing $(E' \mathrm{e}^{\mathrm{i}\omega_f t} \boldsymbol{f}_E + \mathrm{c.c})$, characterized by the frequency ω_f, the amplitude E' and the complex spatial structure $\boldsymbol{f}_E = (f_E, g_E)$. E' may be chosen as a positive real without loss of generality. For the sake of clarity, we will first consider a forcing $\boldsymbol{f}_E$ of Gaussian shape, located near the leading edge of the cavity and which triggers the vertical momentum component

$$\boldsymbol{f}_E = \begin{pmatrix} 0 \\ \alpha \exp(-(x^2 + y^2)/0.1^2) \end{pmatrix}, \tag{3.1}$$

with α such that $\langle \boldsymbol{f}_E, \boldsymbol{f}_E \rangle = 1$. The vertical component of this forcing is represented in figure 3(*a*). Note that it would be possible to consider a more realistic forcing such as blowing/suction (see appendix A for details).

The equations governing the resulting flow field are the same as those given in (2.1) with the additional harmonic forcing $\boldsymbol{f}_E$:

$$\partial_t \boldsymbol{u} + \boldsymbol{u} \cdot \boldsymbol{\nabla} \boldsymbol{u} = -\boldsymbol{\nabla} p + (Re_c^{-1} - \delta') \boldsymbol{\Delta} \boldsymbol{u} + (E' \mathrm{e}^{\mathrm{i}\omega_f t} \boldsymbol{f}_E + \mathrm{c.c}), \quad \boldsymbol{\nabla} \cdot \boldsymbol{u} = \boldsymbol{0}. \tag{3.2}$$

The case of steady forcing and the resonant cases, where the forcing ω_f is close to $\omega_c/2$, ω_c or $2\omega_c$, will be analysed and treated in § 4 and in appendices B and C. In this section, we will consider the non-resonant case. First (§ 3.1), we will show how the harmonic forcing term enters the amplitude equation (2.10). Then (§ 3.2), we will present two control strategies consisting in stabilizing the global mode or shifting the frequency of the flow on the limit cycle. In § 3.3, for a given frequency ω_f, we

will look for the forcing structures $\boldsymbol{f}_E$ that minimize the forcing amplitude E': these forcings, also called the optimal forcings, take advantage of the most sensitive regions of the flow field to trigger the strongest possible responses, the so-called optimal responses. In § 3.4, we will compare the control results to those of a direct numerical simulation conducted at $Re = 6250$ with a harmonic forcing at $\omega_f = 13$. Finally (§ 3.6), we will analyse the meaning of a stability analysis achieved on the resulting mean flows (and not the base flow): in particular, we will see whether the controlled mean flow is stable and whether it reflects the frequency of the controlled flow field.

3.1. *Amplitude equation with harmonic forcing in non-resonant case*

We follow the scalings presented by Fauve (1998) in the case of a forced Van der Pol oscillator. Let us consider a slightly supercritical flow such that $\delta' = \epsilon\delta$, with $\epsilon \ll 1$ and δ being order one. In the non-resonant case, the forcing amplitude satisfies $E' = \epsilon^{1/2}E$ and we consider a flow field of the form

$$\begin{aligned}\boldsymbol{q} = \boldsymbol{q}_0 &+ \epsilon^{1/2}[A\mathrm{e}^{\mathrm{i}\omega_c t}\boldsymbol{q}_A + \text{c.c.}] + \epsilon[\delta\boldsymbol{q}_\delta + |A|^2\boldsymbol{q}_{A\bar{A}} + (A^2\mathrm{e}^{2\mathrm{i}\omega_c t}\boldsymbol{q}_{AA} + \text{c.c.})]\\ &+ \epsilon^{1/2}[E\mathrm{e}^{\mathrm{i}\omega_f t}\boldsymbol{q}_E + \text{c.c.}] + \epsilon[|E|^2\boldsymbol{q}_{E\bar{E}} + (AE\mathrm{e}^{\mathrm{i}(\omega_c+\omega_f)t}\boldsymbol{q}_{AE}\\ &+ A\bar{E}\mathrm{e}^{\mathrm{i}(\omega_c-\omega_f)t}\boldsymbol{q}_{A\bar{E}} + E^2\mathrm{e}^{2\mathrm{i}\omega_f t}\boldsymbol{q}_{EE} + \text{c.c.})]. \end{aligned} \tag{3.3}$$

Introducing this expansion into (3.2), a series of equations is obtained at orders ϵ^0, $\epsilon^{1/2}$ and ϵ. We find that $\boldsymbol{q}_0$, $\boldsymbol{q}_A$, $\boldsymbol{q}_\delta$, $\boldsymbol{q}_{A\bar{A}}$ and $\boldsymbol{q}_{AA}$ are the same as those given in § 2. The flow fields $\boldsymbol{q}_E$, $\boldsymbol{q}_{E\bar{E}}$, $\boldsymbol{q}_{AE}$, $\boldsymbol{q}_{A\bar{E}}$ and $\boldsymbol{q}_{EE}$ are defined by

$$(\mathrm{i}\omega_f\mathscr{P}\mathscr{P}^{\mathrm{T}} + \mathscr{M})\boldsymbol{q}_E = \mathscr{P}(\boldsymbol{f}_E), \tag{3.4}$$

$$\mathscr{M}\boldsymbol{q}_{E\bar{E}} = -\mathscr{P}(\boldsymbol{\nabla u}_E\cdot\overline{\boldsymbol{u}_E} + \overline{\boldsymbol{\nabla u}_E}\cdot\boldsymbol{u}_E), \tag{3.5}$$

$$(\mathrm{i}(\omega_c+\omega_f)\mathscr{P}\mathscr{P}^{\mathrm{T}} + \mathscr{M})\boldsymbol{q}_{AE} = -\mathscr{P}(\boldsymbol{\nabla u}_A\cdot\boldsymbol{u}_E + \boldsymbol{\nabla u}_E\cdot\boldsymbol{u}_A), \tag{3.6}$$

$$(\mathrm{i}(\omega_c-\omega_f)\mathscr{P}\mathscr{P}^{\mathrm{T}} + \mathscr{M})\boldsymbol{q}_{A\bar{E}} = -\mathscr{P}(\boldsymbol{\nabla u}_A\cdot\overline{\boldsymbol{u}_E} + \overline{\boldsymbol{\nabla u}_E}\cdot\boldsymbol{u}_A), \tag{3.7}$$

$$(2\mathrm{i}\omega_f\mathscr{P}\mathscr{P}^{\mathrm{T}} + \mathscr{M})\boldsymbol{q}_{EE} = -\mathscr{P}(\boldsymbol{\nabla u}_E\cdot\boldsymbol{u}_E), \tag{3.8}$$

which consist of non-degenerate linear systems that may readily be inverted (in the non-resonant case, the complex values $\mathrm{i}\omega_f$, 0, $\mathrm{i}(\omega_c+\omega_f)$, $\mathrm{i}(\omega_c-\omega_f)$ and $2\mathrm{i}\omega_f$ do not belong to the spectrum obtained for $Re = 5396$ and shown in figure 2).

Equation (3.4) defines $\boldsymbol{q}_E$ as the linear response of the flow to the forcing $\boldsymbol{f}_E$. For illustration, we represent in figure 3(*b*) the streamwise component of the flow response u_E to a forcing $\boldsymbol{f}_E$ of frequency $\omega_f = 13$ and spatial structure (3.1). We observe that the response is located along the shear layer of the cavity and that it takes advantage of the Kelvin–Helmholtz instability mechanism to trigger energy.

Equation (3.5) yields the zeroth harmonic $\boldsymbol{q}_{E\bar{E}}$ associated to a nonlinear interaction between the forced response $\mathrm{e}^{\mathrm{i}\omega_f t}\boldsymbol{q}_E$ and its complex conjugate. It corresponds to a mean flow distortion analogous to $\boldsymbol{q}_{A\bar{A}}$, but which results from the forcing and not from the global mode. Equations (3.6) and (3.7) involve the structures $\boldsymbol{q}_{AE}$ and $\boldsymbol{q}_{A\bar{E}}$ beating at $\omega_c+\omega_f$ and $\omega_c-\omega_f$, which stem from the nonlinear interaction between the global mode $A\mathrm{e}^{\mathrm{i}\omega_c t}\boldsymbol{q}_A$ and the forced response $E\mathrm{e}^{\mathrm{i}\omega_f t}\boldsymbol{q}_E$ or its complex conjugate. In the case of the forcing $\boldsymbol{f}_E$ defined in (3.1) with frequency $\omega_f = 13$, we show in figure 3(*c–e*) the streamwise components of these three harmonics (the real parts for $\boldsymbol{q}_{AE}$ and $\boldsymbol{q}_{A\bar{E}}$). The size of the structures in each plot reflects its frequency: the zeroth harmonic $\boldsymbol{q}_{E\bar{E}}$ displays large-scale structures, while the $(\omega_c+\omega_f)$- and $(\omega_c-\omega_f)$-harmonics display small-scale features in accordance with their characteristic frequencies $\omega = 7+13 = 20$ and $\omega = 7-13 = -6$. The second harmonic $\boldsymbol{q}_{EE}$ defined in (3.8), which results from the nonlinear interaction of the forced response $E\mathrm{e}^{\mathrm{i}\omega_f t}\boldsymbol{q}_E$ with itself, is not shown here,

and will not be addressed further since this structure does not yield resonance at order $\epsilon^{3/2}$.

At order $\epsilon^{3/2}$, compatibility conditions yield the following equation governing the amplitude $A' = \epsilon^{1/2}A$ of the global mode:

$$\frac{\mathrm{d}A'}{\mathrm{d}t} = [\eta\delta' - \mu(\omega_f)E'^2]A' - \nu A'|A'|^2 . \tag{3.9}$$

This equation is the same as the amplitude equation (2.10), but with an additional term taking into account the effect of the forcing $E'\mathrm{e}^{\mathrm{i}\omega_f t}\boldsymbol{f}_E$ on the amplitude of the global mode A'. This term does not modify the nonlinear saturation term $-A'|A'|^2$ but only the linear dynamics of the global mode: its eigenvalue $\lambda = \mathrm{i}\omega_c + \eta\delta'$ turns into

$$\lambda = \mathrm{i}\omega_c + \eta\delta' - \mu(\omega_f)E'^2 \tag{3.10}$$

when the forcing is switched on. The complex constant $\mu(\omega_f)$ depends on the forcing frequency ω_f and the forcing structure $\boldsymbol{f}_E$, and may be evaluated according to

$$\mu(\omega_f) = \overbrace{\langle \tilde{\boldsymbol{u}}_A, \boldsymbol{\nabla}\boldsymbol{u}_A \cdot \boldsymbol{u}_{E\bar{E}} + \boldsymbol{\nabla}\boldsymbol{u}_{E\bar{E}} \cdot \boldsymbol{u}_A \rangle}^{\mu_{E\bar{E}}(\omega_f)} + \underbrace{\langle \tilde{\boldsymbol{u}}_A, \overline{\boldsymbol{\nabla}\boldsymbol{u}_E} \cdot \boldsymbol{u}_{AE} + \boldsymbol{\nabla}\boldsymbol{u}_{AE} \cdot \overline{\boldsymbol{u}_E} \rangle}_{\mu_{AE}(\omega_f)} + \underbrace{\langle \tilde{\boldsymbol{u}}_A, \boldsymbol{\nabla}\boldsymbol{u}_E \cdot \boldsymbol{u}_{A\bar{E}} + \boldsymbol{\nabla}\boldsymbol{u}_{A\bar{E}} \cdot \boldsymbol{u}_E \rangle}_{\mu_{A\bar{E}}(\omega_f)} . \tag{3.11}$$

This constant involves three contributions $\mu_{E\bar{E}}(\omega_f)$, $\mu_{AE}(\omega_f)$ and $\mu_{A\bar{E}}(\omega_f)$, stemming respectively from the zeroth harmonic $\boldsymbol{u}_{E\bar{E}}$, the $(\omega_c + \omega_f)$-harmonic $\boldsymbol{u}_{AE}$ and the $(\omega_c - \omega_f)$-harmonic $\boldsymbol{u}_{A\bar{E}}$. We will see (§ 3.6) that the respective magnitudes of these three terms have some direct influence on the stability of the resulting mean flows.

3.2. *Control strategies*

As mentioned in the previous section, the harmonic forcing $E'\mathrm{e}^{\mathrm{i}\omega_f t}\boldsymbol{f}_E$ modifies the amplification rate and frequency of the global mode. The amplification rate reads

$$\sigma = \eta_r\delta' - \mu_r(\omega_f)E'^2. \tag{3.12}$$

Let us consider a supercritical Reynolds number $Re > Re_c$, so that $\delta' > 0$. Since $\eta_r > 0$, the global mode is unstable in the case of no control ($E' = 0$). A forcing at a given frequency ω_f may stabilize the global mode if $\mu_r(\omega_f) > 0$ and the forcing amplitude E'_s that achieves exact stabilization ($\sigma = 0$) of the global mode reads

$$E'_s = \sqrt{\frac{\eta_r}{\mu_r(\omega_f)}\delta'}. \tag{3.13}$$

The stabilization amplitude is proportional to the square root of the distance to criticality δ'. E'_s only exists if $\mu_r(\omega_f) > 0$ and depends on the frequency ω_f: the higher $\mu_r(\omega_f)$, the lower E'_s. In the case of the fixed forcing $\boldsymbol{f}_E$ given in (3.1), we may compute $\mu_r(\omega_f)$ for forcing frequencies within $0 \leqslant \omega_f \leqslant 15$ (it has been checked that for higher frequencies $|\mu_r(\omega_f)|$ becomes very small, leading to inefficient control strategies). The sign of $\mu_r(\omega_f)$ and its absolute value, respectively, are shown with dashed and solid lines in figure 4(*a*), the thick black vertical lines representing the resonant frequencies $\omega_c/2$, ω_c and $2\omega_c$ that are not allowed here. We see that for nearly all frequencies the control has a stabilizing effect $\mu_r(\omega_f) > 0$. Also, there are preferred frequencies for the control: leaving aside the dominant peak that is observed at the resonant frequency (which is not allowed here), it is seen that the curve $|\mu_r(\omega_f)|$

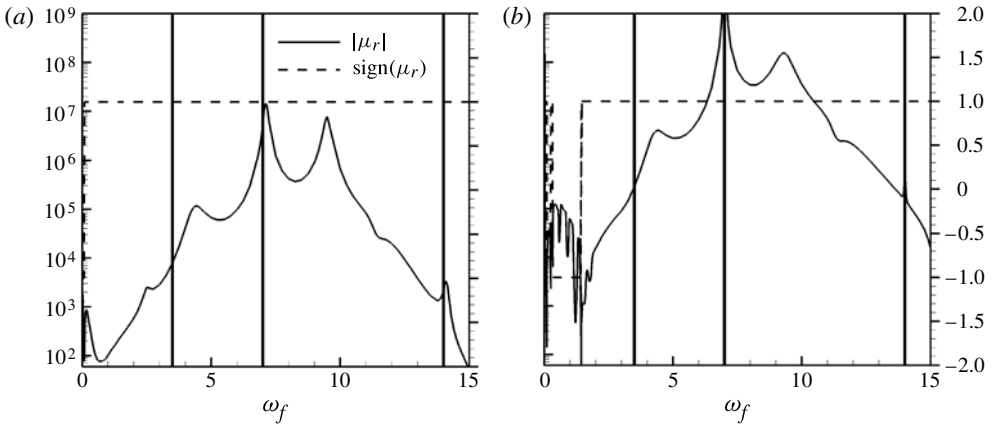

FIGURE 4. Behaviour as a function of ω_f of coefficient $\mu_r(\omega_f)$ involved in the amplification rate of controlled flow (see (3.12)). Solid line, $|\mu_r(\omega_f)|$; dashed line, sign$(\mu_r(\omega_f))$. (*a*) With fixed forcing defined in (3.1); (*b*) with optimal forcings. The two figures share the same axes: the solid lines go with the *y*-axis of (*a*), and the dashed lines go with the *y*-axis of (*b*).

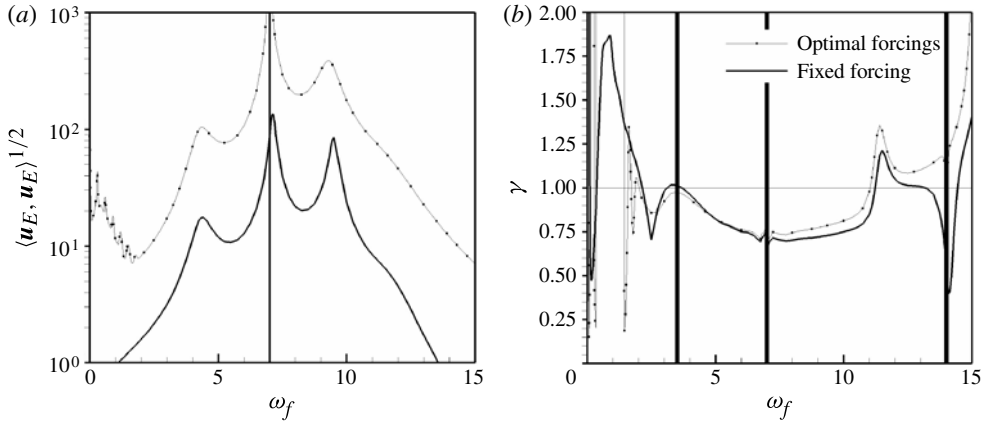

FIGURE 5. (a) Amplitude of response $\boldsymbol{u}_E$ triggered by unit energy forcing $\boldsymbol{f}_E$ as a function of forcing frequency ω_f. (*b*) Ratio r between r.m.s. of fluctuating kinetic energy at $(x = 0.75, y = 0)$ with global mode stabilization strategy and the same quantity without control. This quantity is only defined when the forcing is stabilizing ($\mu_r(\omega_f) > 0$). If not ($\mu_r(\omega_f) < 0$), then the value of r is set to an arbitrarily large value. Thick black line, with fixed forcing defined in (3.1); grey line with symbols, with optimal forcings.

displays local maxima near $\omega_f = 4.5$ and $\omega_f = 9.2$. This may be explained by analysing the energy of the forced response $\langle \boldsymbol{u}_E, \boldsymbol{u}_E \rangle$ as a function of frequency ω_f. The square root of this quantity is represented in figure 5(*a*) by a thick solid line. We see that the same forcing structure may yield different energy responses depending on the forcing frequency ω_f: for example, frequencies around $\omega_f = 4.5$ and $\omega_f = 9.2$ are particularly sensitive. This probably stems from the existence of two weakly damped global modes in the vicinity of these frequencies. These two global modes (together

with the marginal global mode) belong to a group of modes that become unstable as the Reynolds number is increased. In the spectrum, the eigenvalues of the global modes belonging to this group are aligned on a parabolic curve (see Barbagallo, Sipp & Schmid 2009 for more details). As the Reynolds number increases, these global modes become unstable due to a Rossiter-like feedback mechanism (Rossiter 1962), which involves the convective Kelvin–Helmholtz instability mechanism and an instantaneous pressure feedback (due to the incompressibility of the flow). If the forcing frequency ω_f matches one of those of these global modes, than the flow response $\boldsymbol{u}_E$ may take advantage of these instability mechanisms and display a strong energy. From the definition of $\mu(\omega_f)$ given in (3.11), it is clear that a stronger $\boldsymbol{u}_E$ generally yields a larger $|\mu_r(\omega_f)|$. Note finally that the global mode stabilization strategy does not mean suppression of unsteadiness over all frequencies. Indeed, when stabilization occurs, the harmonic forcing term $\epsilon^{1/2}[E\mathrm{e}^{\mathrm{i}\omega_f t}\boldsymbol{q}_E + \text{c.c.}]$ and its harmonics remain non-zero in expansion (3.3): this shows that the resulting flow exhibits harmonic flow oscillations at frequencies close to ω_f, $2\omega_f$, and so on. If the forcing frequency ω_f is superior to ω_c, the stabilization strategy ensures suppression of unsteadiness on the frequency range $0 \leqslant \omega < \omega_f$. To nonetheless assess the control efficiency over all frequencies, we may compare the oscillation amplitudes of the flow with and without control. If control is applied, the dominant harmonic term in the flow solution is $E'\mathrm{e}^{\mathrm{i}\omega_f t}\mathbf{q}_E + \text{c.c}$ with $E' = E'_s$ given in (3.13). Without control, the dominant term is $A'\mathrm{e}^{\mathrm{i}\omega_c t}\mathbf{q}_A + \text{c.c}$ with $|A'| = |A'|^{LC}$ given in (2.15). To be more specific, let us consider the r.m.s. (root mean square) of the mean fluctuating kinetic energy in the shear layer at the spatial location $(x = 0.75, y = 0)$. Comparison of this quantity with and without control may be achieved by considering the ratio

$$r = \frac{\|\boldsymbol{u}_E(0.75, 0)\|}{\|\boldsymbol{u}_A(0.75, 0)\|} \frac{E'_s}{|A'|^{LC}}, \tag{3.14}$$

where $\|\boldsymbol{u}\| = (|u|^2 + |v|^2)^{1/2}$ is the norm of the velocity (at some given spatial location). If $r < 1$ (respectively $r > 1$), then the control reduces (respectively strengthens) the r.m.s. of the mean fluctuating kinetic energy at $(x = 0.75, y = 0)$. The quantity r is dependent on the forcing frequency through the terms $\|\boldsymbol{u}_E(0.75, 0)\|$ and E'_s. It is represented in figure 5(*b*) by a thick solid line as a function of the forcing frequency. We observe that the velocity oscillation amplitudes may be reduced by approximately 20 % if the forcing frequency lies within the frequency range $5 < \omega_f < 11$ and nearly 50 % in a narrow band around $\omega_f \approx 0.2$. These relatively weak reductions of the flow oscillation amplitudes show that the global mode stabilizing strategy is not fully relevant when one aims at suppressing fluctuations over all frequencies.

The second control strategy only aims at shifting the frequency of the flow field on the limit cycle. In this case, the amplification rate of the global mode is still unstable $\sigma = \eta_r \delta' - \mu_r(\omega_f)E'^2 > 0$ and the flow is still located on a limit cycle. However, the amplitude of the oscillations has changed,

$$|A'| = \sqrt{\frac{\eta_r \delta' - \mu_r(\omega_f)E'^2}{\nu_r}}, \tag{3.15}$$

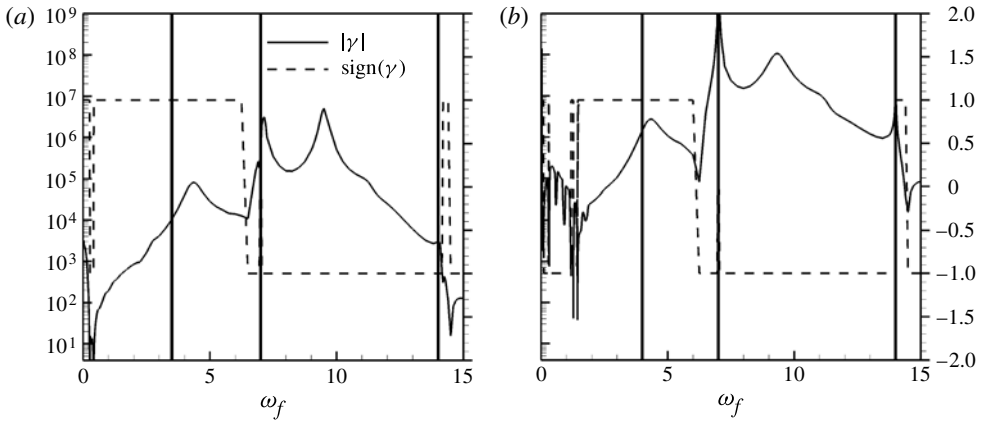

FIGURE 6. Behaviour as a function of ω_f of coefficient $\gamma(\omega_f)$ involved in limit cycle frequency of controlled flow (see (3.16)). Solid line, $|\gamma|$; dashed line, sign(γ). (*a*) With fixed forcing defined in (3.1); (*b*) with optimal forcings. The two figures share the same axes: the solid lines go with the *y*-axis of (*a*), and the dashed lines go with the *y*-axis of (*b*).

and the frequency of the flow field now reads

$$\omega^{LC} = \omega_c + \eta_i\delta' - \frac{\eta_r}{\nu_r}\nu_i\delta' + \underbrace{\mu_r(\omega_f)\left(-\frac{\mu_i(\omega_f)}{\mu_r(\omega_f)} + \frac{\nu_i}{\nu_r}\right)}_{\gamma(\omega_f)} E'^2. \tag{3.16}$$

The three first terms on the right-hand side correspond to the frequency of the flow field without control (see (2.16)). The last term corresponds to the frequency shift due to the forcing. It is proportional to the square of the forcing amplitude E' and to the quantity $\gamma(\omega_f)$ defined in the braces of (3.16). The sign of $\gamma(\omega_f)$ determines whether the control will increase or decrease the frequency of the flow on the limit cycle. In figure 6(*a*), we represent, for the fixed forcing structure $\boldsymbol{f}_E$ defined in (3.1), the sign (dashed line) and amplitude (solid line) of γ as a function of the forcing frequency ω_f. It is seen that the forcing decreases the frequency of the flow for high frequencies $6.2 \leqslant \omega_f \leqslant 14$ and increases it for lower frequencies $0.5 \leqslant \omega_f \leqslant 6.2$. Also, the curve is seen to display local extrema that are located at the same places as the local extrema of $|\mu_r(\omega_f)|$ (see figure 4*a*). This again shows the marked sensitivity of the flow to forcing at these particular frequencies.

3.3. *Optimal forcings/optimal responses*

In order to manipulate the flow at minimum expense, we need to find forcings $\boldsymbol{f}_E$ of unit energy $\langle \boldsymbol{f}_E, \boldsymbol{f}_E \rangle = 1$ that generate strong coefficients $|\mu_r(\omega_f)|$ and $|\gamma(\omega_f)|$. As a first step in this direction, we consider the optimal forcing $\boldsymbol{f}_E$ of unit energy that yields the strongest possible energy $\langle \boldsymbol{u}_E, \boldsymbol{u}_E \rangle^{1/2}$. The corresponding response $\boldsymbol{q}_E$ is referred to as the optimal response. Its energy $\langle \boldsymbol{u}_E, \boldsymbol{u}_E \rangle$ corresponds to the optimal energy gain at a prescribed frequency ω_f. Such an optimization problem may be solved thanks to Lanczos methods (see Lehoucq & Sorensen 1996, Alizard & Robinet 2007, Monokrousos *et al.* 2010, Brandt *et al.* 2011 and Sipp *et al.* 2010). We use the ARPACK library in regular mode and repeatedly evaluate $\tilde{\mathscr{R}}\mathscr{R}$ on some arbitrary vector. Here, $\tilde{\mathscr{R}}$ and $\mathscr{R}$ are respectively the adjoint and direct resolvent

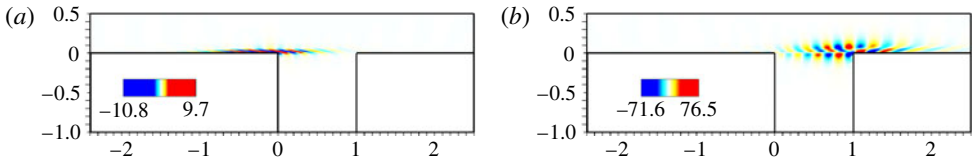

FIGURE 7. (*a*) Streamwise component $\mathrm{Re}(f_E)$ of unit energy optimal forcing for $\omega_f = 13$; (*b*) streamwise component $\mathrm{Re}(u_E)$ of associated optimal response. These figures may be compared to those of the fixed forcing case shown in figure 3(*a*,*b*).

operators $(-\mathrm{i}\omega\mathscr{P}\mathscr{P}^{\mathrm{T}} + \tilde{\mathscr{M}})^{-1}$ and $(\mathrm{i}\omega\mathscr{P}\mathscr{P}^{\mathrm{T}} + \mathscr{M})^{-1}$. For details of implementation, the reader is referred to Sipp & Marquet (2012). The square root of the optimal energy gain is represented as a function of frequency by a grey line with symbols in figure 5(*a*). We obtain results that are similar to those of the fixed forcing case (black line): the peaks are located at the same frequencies but the optimal responses display amplitudes which are at least one order of magnitude higher than the responses triggered by the fixed forcing given in (3.1). The optimal forcings are all located near the leading edge of the cavity and display structures that lay against the stream to take advantage of the Orr mechanism to extract energy of the flow. The higher the frequency, the finer the spatial scales of the forcing. Hence, the spatial location and overall shape of the optimal forcings are only weakly dependent on the frequency. This may explain qualitatively why the curves in figure 5(*a*) for the fixed forcing and for the optimal forcings are just shifted by an order of magnitude, which looks surprising at first glance. Also, it may be shown that, near the frequencies of the global modes belonging to the parabolic curve mentioned in § 3.2, the optimal forcings display a structure close to the corresponding adjoint global modes. This holds in particular at the frequencies $\omega_f = 4.5$, $\omega_f = 9.2$ and near $\omega_f = 7.0$. In the case $\omega_f = 13$, we show in figure 7(*a*,*b*) the real parts of the streamwise component of the optimal forcing and response structures. The optimal forcing is normalized to unit energy while the optimal response verifies $\langle \boldsymbol{u}_E, \boldsymbol{u}_E \rangle = 516$, which may be compared to the energy of the response in the case of the fixed forcing $\langle \boldsymbol{u}_E, \boldsymbol{u}_E \rangle = 1.73$.

We may then compute for all frequencies the harmonics shown in figure 3 and the coefficients $|\mu_r(\omega_f)|$ and $|\gamma(\omega_f)|$ characterizing the control efficiency of the chosen forcings $\boldsymbol{f}_E$. Figures 4(*b*) and 6(*b*) show that the coefficients $|\mu_r(\omega_f)|$ and $|\gamma(\omega_f)|$ stemming from the optimal forcings display values that are at least one order of magnitude higher than those related to the fixed forcing case (3.1). The optimal forcings therefore yield for all frequencies forcing amplitudes E' that are an order of magnitude lower than those required by the fixed forcing structure given in (3.1). For example, at $\omega_f = 13$, $\mu_r = 5.8 \times 10^6$ for the optimal forcing, and $\mu_r = 3.8 \times 10^3$ for the fixed forcing. In figure 5(*b*), we use a grey line with symbols for the parameter r (see (3.14)), indicating whether the stabilizing control strategy achieves ($r < 1$) or does not achieve ($r > 1$) a net reduction of the mean fluctuating kinetic energy at the spatial location ($x = 0.75, y = 0$). It is seen that the optimal forcings yield slightly larger values of r than in the case of the fixed forcing, especially at high frequencies $\omega_f > 7$. Hence, the fixed forcing defined in (3.1) should be slightly favoured to achieve a net reduction of the oscillation amplitudes. There is no contradiction here since the optimal forcings have been designed to lower the stabilizing forcing amplitude E'_s and not to reduce r. Also, there seem to exist very narrow frequency bands where the

net reduction of mean fluctuating kinetic energy may reach values of $r = 0.2$ near $\omega_f \approx 0.07$, 0.31 and 1.45.

3.4. *Comparison with DNS at Re = 6250*

In this section, we compare the results of the asymptotic analysis presented in §§ 3.1 and 3.2 to direct numerical simulation (DNS). The DNS code marches in time the governing equations (3.2) using the primitive variables (u, v, p). We use the same mesh and spatial discretizations as in the previous sections. The pressure field is obtained thanks to the Uzawa algorithm preconditioned by the Cahouet–Chabart method (Glowinski 2003). The time discretization is semi-implicit and based on a second-order backward differentiation formula scheme. The time step in the simulations is $\Delta t = 0.002$.

At each time, we extract the following quantity from the DNS: $\tilde{A}'(t) = \langle \tilde{\boldsymbol{u}}_A, \boldsymbol{u}(t) - \boldsymbol{u}_0 \rangle$, where $\tilde{\boldsymbol{u}}_A$ is the adjoint marginal global mode shown in figure 1(*d*) and $\boldsymbol{u}_0$ the base flow at $Re = 5396$. Inspection of asymptotic expansion (3.3) shows that at leading order, $\tilde{A}'(t)$ should behave as

$$\tilde{A}'(t) = A' \mathrm{e}^{\mathrm{i}\omega_c t} + \langle \tilde{\boldsymbol{u}}_A, \boldsymbol{u}_E \rangle E' \mathrm{e}^{\mathrm{i}\omega_f t} + \langle \tilde{\boldsymbol{u}}_A, \overline{\boldsymbol{u}_E} \rangle E' \mathrm{e}^{-\mathrm{i}\omega_f t}. \tag{3.17}$$

This stems from the fact that $\langle \tilde{\boldsymbol{u}}_A, \boldsymbol{u}_A \rangle = 1$ and $\langle \tilde{\boldsymbol{u}}_A, \overline{\boldsymbol{u}_A} \rangle = 0$. Also, it is possible to evaluate numerically the complex constants $\langle \tilde{\boldsymbol{u}}_A, \boldsymbol{u}_E \rangle = -4.49 + 1.51\mathrm{i}$ and $\langle \tilde{\boldsymbol{u}}_A, \overline{\boldsymbol{u}_E} \rangle = 0.16 - 0.0096\mathrm{i}$.

The test case is as follows. We choose a supercritical Reynolds number $Re = 6250$ where the base flow displays a single unstable global mode (see the symbols in figure 2). In the case of no control, the flow field should exhibit an oscillatory movement characterized by an amplitude $|A'|$ given by (2.15). We obtain $|A'| = 0.0174$. The quantity $\tilde{A}'(t)$ reduces to the first term on the right-hand side of (3.17) and therefore corresponds to the amplitude of the global mode. The DNS simulation recovers this uncontrolled situation quite accurately, as shown in figure 8(*a*). Here, the amplitude of the global mode $\mathrm{Re}(\tilde{A}'(t))$ as obtained in the DNS is represented as a function of time. Up to $t = 92.2$, the control is switched off: the global mode is seen to oscillate with an amplitude which is in agreement with the value $|A'| = 0.0174$ given by the theory (see the horizontal lines on the left of the figure). In figure 8(*b*), we have represented as a function of time the local frequency of the oscillations shown in figure 8(*a*): the global mode is seen to oscillate at frequency $\omega = 7.23$, which is close to the value $\omega^{LC} = 7.162$ predicted by theory in (2.16).

We would now like to stabilize the global mode by a high-frequency forcing, which should stabilize the flow over all frequencies below the forcing frequency ω_f. We choose a harmonic forcing of frequency $\omega_f = 13$ with the optimal forcing structure shown in figure 7(*a*). This control should stabilize the flow (μ_r is strictly positive) at a still reasonable cost (E'_s is small since $\mu_r = 5.8 \times 10^5$ is an order of magnitude larger than $\eta_r = 4688.43$) over frequencies up to nearly twice the natural frequency of the flow ($\omega_f/\omega_c \approx 1.86$). Also, the choice $\omega_f = 13$ ensures that the harmonics produced by the applied forcing ($\omega = 0, \pm\omega_f, \pm 2\omega_f, \pm(\omega_c + \omega_f), \pm(\omega_c - \omega_f)$) are not too close to the resonant frequencies $\pm\omega_c = \pm 7.0$. In particular, $\omega_c - \omega_f = -6.0$, which is reasonably far away from $-\omega_c = -7.0$. The amplitude E' is chosen as the threshold stabilizing amplitude E'_s given in (3.13): $E' = 0.000453$. In figure 8(*a*,*b*), the control is switched on at $t = 92.2$. We observe that the amplitude of the oscillations decreases from 0.017 to approximately 0.002 and that the frequency of the oscillations rises to the forcing frequency $\omega_f = 13$. This is in accordance with the behaviour predicted by theory. In

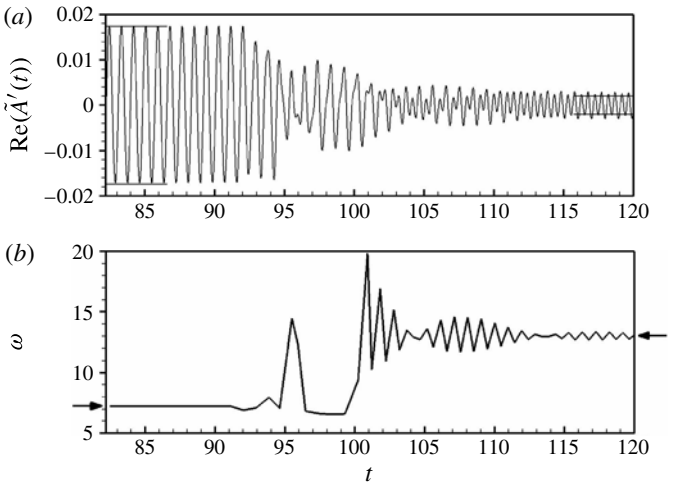

FIGURE 8. DNS at $Re = 6250$. Control is switched on at $t = 92.2$ and is characterized by a forcing frequency $\omega_f = 13$, an amplitude $E' = E'_s = 0.000453$ (see (3.13)) and $\boldsymbol{f}_E$ as the optimal forcing. (*a*) Amplitude $\mathrm{Re}(\tilde{A}'(t))$ as a function of time. The horizontal lines refer to the values predicted by the amplitude equation (3.9): the two lines on the left refer to the uncontrolled situation and the two on the right refer to the controlled situation. (b) The local frequency associated to signal $\mathrm{Re}(\tilde{A}'(t))$ is shown as a function of time. For this, an algorithm tracks the occurrence in time of three consecutive extrema t_0, t_1 and t_2: t_0 is reported on the x-axis and $\omega = 2\pi/(t_2 - t_0)$ on the y-axis. The two arrows respectively represent the natural frequency of the flow $\omega = 7.23$ and the forcing frequency $\omega_f = 13$. The movie available at http://dx.doi.org/10.1017.jfm.2012.329 represents the vorticity of the flow field and the cross-stream velocity at the point $(x = 0.75, y = 0)$ during the same time range.

(3.17), the quantity $\tilde{A}'(t)$ is governed by the two last terms of the right-hand side, since $|A'| \to 0$ as $t \to \infty$ (the global mode is stabilized). With the numerical values given earlier, the resulting oscillations of $\mathrm{Re}(\tilde{A}'(t))$ should display an amplitude of 0.002 and a frequency of $\omega_f = 13$. This is exactly what is observed in the DNS.

In figure 9, we show a spectrum of the cross-stream velocity component extracted in the shear layer at position $(x = 0.75, y = 0)$. The solid and dashed lines, respectively, refer to the uncontrolled and controlled DNS simulations. In the uncontrolled case, we observe several peaks: the dominant peak at frequency $\omega = 7.23$ is related to the saturated global mode $A\mathrm{e}^{\mathrm{i}\omega_c t}\boldsymbol{u}_A + \mathrm{c.c.}$, the second at frequency $\omega = 14.4$ is related to the second harmonic $A^2\mathrm{e}^{2\mathrm{i}\omega_c t}\boldsymbol{u}_{AA} + \mathrm{c.c.}$, and the others are related to higher-order harmonics. In the controlled case, we can see that the unsteadiness near the frequency $\omega = 7.23$ has completely disappeared: the global mode has effectively been damped. Only the forcing frequency $\omega_f = 13$ and its harmonics remain in the spectrum. This validates the analysis of §§ 3.1 and 3.2.

3.5. *Relevance of asymptotic analysis as ϵ increases*

The theoretical study performed in this paper is strictly valid only in the close vicinity of the bifurcation $\epsilon \ll 1$. In the previous section we checked that the asymptotic approach is still close to the true nonlinear solution for the non-infinitesimal value $\epsilon = 1/5396 - 1/6250 = 2.5 \times 10^{-5}$. This success can be explained qualitatively by the following observation: in figure 2, it is seen that the spectrum at $Re = 6250$

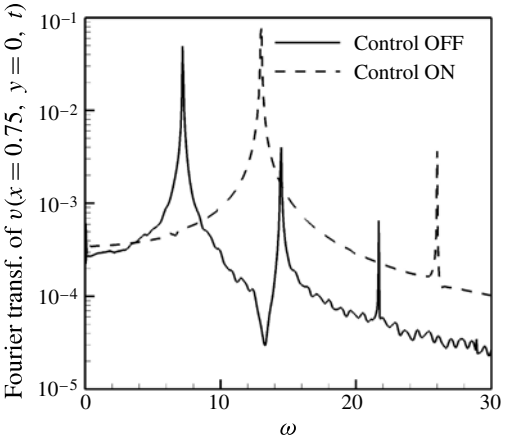

FIGURE 9. Spectrum of $v(x = 0.75, y = 0, t)$ in DNS at $Re = 6250$. Solid line, without control; dashed line, with control, characterized by $\omega_f = 13$, $E' = E'_s = 0.000453$ and $\boldsymbol{f}_E$ as optimal forcing. The spectra were computed on the time series $120 \leqslant t \leqslant 215$ after the transient has died away (the control was switched on at $t = 92.2$).

still displays only one unstable global mode (the global mode that was marginal at $Re = 5396$) while all other modes are strictly damped. This spectrum is therefore qualitatively close to the one obtained for $0 < \epsilon \ll 1$, which explains why the asymptotic approach is capable of handling the small and smooth variations between the dynamics at $Re = 6250$ and $Re = 5396$. However, if one selects an even higher Reynolds number, a second global mode will eventually become marginal: such an event, which has not been accounted for explicitly in the theoretical analysis, will certainly compromise the quality of the present asymptotic solution. A qualitative change in the dynamics at some Reynolds number therefore stands as a limit for the validity of the present asymptotic approach. The presence of weakly damped global modes in the dynamics can therefore be viewed as a strength of control efficiency (the preferred frequencies for control at $\omega = 4.5$ and $\omega = 9.2$ are due to the presence of such modes) and also as a weakness, since they may limit the validity domain of the analysis in Reynolds number.

In the case when two global modes display close bifurcation thresholds (which means that at the bifurcation threshold of the least damped global mode the other global mode is just weakly damped), we are in fact faced with a bifurcation of higher codimension. As shown by Meliga *et al.* (2009), a shift operator may then be introduced to tackle the problem in a nearly rigorous way. In so doing, one would obtain two coupled amplitude equations describing the dynamics of the two nearly marginal global modes. For example, it would be interesting to determine, for a slightly supercritical Reynolds number, whether a stabilizing control designed for the weakly unstable global mode could destabilize the weakly damped global mode.

Finally, note that the purpose of the present asymptotic analysis is only to exhibit a particular solution of the Navier–Stokes equations. The analysis does not show that the true nonlinear dynamics in the presence of a richer perturbation environment (three-dimensional perturbations for example) obligatorily follows the dynamics prescribed by the asymptotic analysis. For example, transient effects associated to the amplification of upstream noise by convective instabilities could drive the flow towards other solutions.

3.6. *Mean flow and stability*

The mean flow $\boldsymbol{u}^{MF}$ corresponds to the time-average of the unsteady flow field given in (3.3):

$$\boldsymbol{u}^{MF} = \boldsymbol{u}_0 + \delta'\boldsymbol{u}_\delta + E'^2\boldsymbol{u}_{E\bar{E}} + |A'|^2\boldsymbol{u}_{A\bar{A}}. \tag{3.18}$$

To study the stability of the mean flow, we follow the developments presented in Sipp & Lebedev (2007). It may be shown that the complex value

$$\lambda^{MF} = \mathrm{i}\omega_c + \eta\delta' - \mu_{E\bar{E}}(\omega_f)E'^2 - \nu_{A\bar{A}}|A'|^2 \tag{3.19}$$

belongs to the spectrum of the Jacobian derived around the mean flow $\boldsymbol{u}^{MF}$. More precisely, the result states that the quantity $\mathrm{e}^{\lambda^{MF}t}\boldsymbol{u}_A$ (where $\boldsymbol{u}_A$ is the global mode defined in (2.4)) is a solution of the Navier–Stokes equations (2.1) linearized around $\boldsymbol{u}^{MF}$. The complex constant $\mu_{E\bar{E}}(\omega_f)$ is defined in (3.11) and is related to the zeroth harmonic $\boldsymbol{q}_{E\bar{E}}$ generated by the forcing response $\boldsymbol{q}_E$. The complex constant $\nu_{A\bar{A}}$ defined in (2.12) is analogous but linked to the zeroth harmonic $\boldsymbol{q}_{A\bar{A}}$ generated by the global mode $\boldsymbol{q}_A$.

In the case of no control, we retrieve the results in Sipp & Lebedev (2007). In this case, $E' = 0$, and the saturation amplitude on the limit cycle $|A'|$ is given in (2.15). Considering the real and imaginary parts of (3.19) yields

$$\sigma^{MF} = \left(1 - \frac{\nu_{A\bar{A}r}}{\nu_r}\right)\eta_r\delta', \tag{3.20}$$

$$\omega^{MF} = \omega_c + \eta_i\delta' - \frac{\eta_r}{\nu_r}\nu_{A\bar{A}i}\delta'. \tag{3.21}$$

Hence, if $\nu_{A\bar{A}r} \approx \nu_r$, then the mean flow is marginally stable ($\sigma^{MF} \ll \eta_r\delta'$). Comparison of ω^{MF} with ω^{LC} (see (2.16)) shows that, if $\nu_{A\bar{A}i} \approx \nu_i$, then the mean flow displays the frequency of the flow on the limit cycle. These conditions state that the zeroth harmonic $\boldsymbol{u}_{A\bar{A}}$ is much stronger than the second harmonic $\boldsymbol{u}_{AA}$. In the present case, we have $\nu_{A\bar{A}r} = 270.01$, $\nu_r = 390.27$ and $\nu_{A\bar{A}i} = -155.45$, $\nu_i = -142.91$, which shows that the mean flow is not exactly marginally stable but that its frequency matches the frequency of the flow on the limit cycle reasonably well.

In the case $|A'| \ll 1$, we obtain a physical interpretation of a linear stability analysis applied to the mean flow (and not to the base flow). Indeed, if $|A'| \ll 1$, the dynamics of the global mode in the presence of forcing is linear, and governed by the eigenvalue given in (3.10). Comparison with (3.19) (and considering $|A'| \ll 1$) shows that $\lambda = \lambda^{MF}$ if $\mu(\omega_f) \approx \mu_{E\bar{E}}(\omega_f)$. If this condition holds, then the linear dynamics of the global mode in the presence of forcing is governed by an eigenvalue stemming from a mean flow analysis and not from a base flow analysis. To the author's knowledge this is the first result justifying the use of a mean flow for a linear stability analysis, in the sense that an eigenvalue of the mean flow (and not of the base flow) will effectively govern the linear dynamics of an eigenmode. Further, in this perspective it is worth noting that $\mu_{E\bar{E}}(\omega_f)$ may be linked to the sensitivity maps introduced by Marquet *et al.* (2008*a*). Indeed, after performing some integration by parts, $\mu_{E\bar{E}}(\omega_f) = -\langle \boldsymbol{\nabla}_{\boldsymbol{u}_0}\lambda, \boldsymbol{u}_{E\bar{E}}\rangle$, where $\boldsymbol{\nabla}_{\boldsymbol{u}_0}\lambda = \boldsymbol{\nabla}\tilde{\boldsymbol{u}}_A \cdot \overline{\boldsymbol{u}_A} - (\boldsymbol{\nabla}\boldsymbol{u}_A)^* \cdot \tilde{\boldsymbol{u}}_A$ is the sensitivity of the eigenvalue λ with respect to a modification of the base flow $\boldsymbol{u}_0$ (Marquet *et al.* 2008*a*).

We will now examine the stability properties of the mean flow in the case of the two control strategies presented in § 3.2.

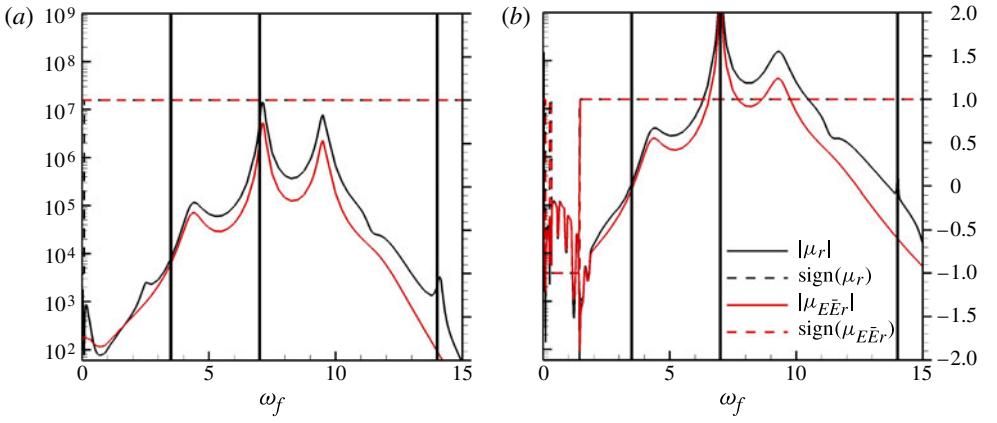

FIGURE 10. Assessment of mean flow stability. Black solid line, $|\mu_r(\omega_f)|$; black dashed line, $\text{sign}(\mu_r(\omega_f))$; red solid line, $|\mu_{E\bar{E}r}(\omega_f)|$; red dashed line, $\text{sign}(\mu_{E\bar{E}r}(\omega_f))$. (*a*) With fixed forcing defined in (3.1); (*b*) with optimal forcings. The two figures share the same axes: the black and red solid lines go with the *y*-axis of (*a*), and the black and red dashed lines go with the *y*-axis of (*b*).

3.6.1. *Stabilization strategy*

In the stabilization strategy, the forcing amplitude E' is given in (3.13) and the amplitude of the marginal global mode is zero ($|A'| = 0$). Hence, the amplification rate induced by a mean flow stability analysis (obtained by taking the real part of (3.19)) simplifies to

$$\sigma^{MF} = \left(1 - \frac{\mu_{E\bar{E}r}(\omega_f)}{\mu_r(\omega_f)}\right) \eta_r \delta'. \tag{3.22}$$

Hence, if $\mu_{E\bar{E}r}(\omega_f) \approx \mu_r(\omega_f)$, then the mean flow is marginally stable $\sigma^{MF} \ll \eta_r \delta'$. This condition states that the zeroth harmonic $\boldsymbol{u}_{E\bar{E}}$ is much stronger than the $(\omega_c + \omega_f)$-harmonic $\boldsymbol{u}_{AE}$ and the $(\omega_c - \omega_f)$-harmonic $\boldsymbol{u}_{A\bar{E}}$. In figure 10, we have checked whether this condition holds in the case of the fixed forcing (figure 10*a*) and in the case of the optimal forcings (figure 10*b*). In each plot, we use black solid and red solid lines, respectively, to show the quantities $|\mu_r(\omega_f)|$ and $|\mu_{E\bar{E}r}(\omega_f)|$ as a function of the forcing frequency ω_f. The black dashed and red dashed lines refer to the signs of $\mu_r(\omega_f)$ and $\mu_{E\bar{E}r}(\omega_f)$. The resulting mean flow is stable if the black lines coincide with the solid lines. Except in the case of low-frequency optimal forcings (figure 10*b* for $\omega_f < 2$), we can see that this is not the case, which shows that the mean flows resulting from a stabilization strategy are not marginally stable. From a physical point of view, this shows that the stabilization mechanisms involved here are not related to mean flow distortions but are linked to the dynamics of the $(\omega_c + \omega_f)$- and $(\omega_c - \omega_f)$-harmonics.

3.6.2. *Frequency shift strategy*

In the frequency shift strategy, the flow is located on a limit cycle whose amplitude $|A'|$ is given in (3.15). The frequency ω^{MF} induced by a mean flow stability analysis (imaginary part of (3.19)) simplifies to

$$\omega^{MF} = \omega_c + \eta_i \delta' - \frac{\eta_r}{\nu_r} \nu_{A\bar{A}i} \delta' + \mu_r(\omega_f) \left(-\frac{\mu_{E\bar{E}i}(\omega_f)}{\mu_r(\omega_f)} + \frac{\nu_{A\bar{A}i}}{\nu_r}\right) E'^2. \tag{3.23}$$

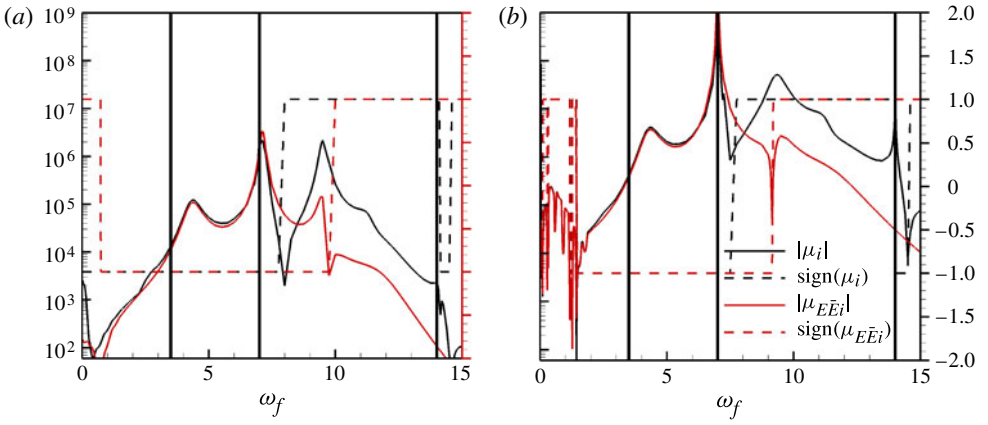

FIGURE 11. Assessment of mean flow stability. Black solid line, $|\mu_i(\omega_f)|$; black dashed line, $\text{sign}(\mu_i)(\omega_f)$; red solid line, $|\mu_{E\bar{E}i}(\omega_f)|$; red dashed line, $\text{sign}(\mu_{E\bar{E}i}(\omega_f))$. (*a*) With fixed forcing defined in (3.1); (*b*) with optimal forcings. The two figures share the same axes: the solid lines go with the *y*-axis of (*a*), and the dashed lines go with the *y*-axis of (*b*).

This frequency may be compared to the frequency of the flow on the limit cycle, given in (3.16). It is seen that the two frequencies match if $\nu_{A\bar{A}i} \approx \nu_i$ and $\mu_{E\bar{E}i}(\omega_f) \approx \mu_i(\omega_f)$. Recalling that $\nu_{A\bar{A}i} = -155.45$ and $\nu_i = -142.91$, we conclude that the first condition is approximately satisfied. For the second one, we have represented in figure 11 the quantities $|\mu_i(\omega_f)|$, $|\mu_{E\bar{E}i}(\omega_f)|$, $\text{sign}(\mu_i(\omega_f))$ and $\text{sign}(\mu_{E\bar{E}i}(\omega_f))$ as a function of the forcing frequency ω_f. We have used the same style and colour conventions as in figure 10. Figure 11(*a*) refers to the fixed forcing case and figure 11(*b*) the optimal forcings case. We observe that the black and red curves match for frequencies $\omega_f < 7$ and that they are different for higher frequencies. This shows that the resulting mean flow exhibits a global mode of frequency equal to the frequency of the flow on the limit cycle only for low-frequency forcings $\omega_f < 7$, while this is not the case for high-frequency forcings $\omega_f > 7$. From a physical point of view, this shows that, depending on the forcing frequencies, sometimes it is the mean flow distortion that is responsible for the frequency shift, and sometimes it is the $(\omega_c + \omega_f)$- and $(\omega_c - \omega_f)$-harmonics.

4. Forcing near particular frequencies

When the forcing frequency ω_f is chosen close to 0, $\omega_c/2$, ω_c or $2\omega_c$, then the scaling and development introduced in § 3.1 are no longer valid. Indeed, the linear systems in (3.4), (3.6) and (3.7) or (3.8) may then be degenerate. As shown in Fauve (1998), different scalings are required. The cases where the forcing frequency ω_f is close to $\omega_c/2$ or $2\omega_c$ are treated in appendices B and C. In the next two sections (§§ 4.1 and 4.2), we will present the case of forcing near the natural frequency of the flow ($\omega_f \approx \omega_c$) and the case of steady forcing ($\omega_f = 0$).

4.1. *Forcing near* $\omega_f = \omega_c$

Here we focus on the case where the forcing frequency ω_f is close to the frequency ω_c of the marginal global mode: $\omega_f = \omega_c + \Omega'$ with Ω' as a real. If $\delta' = \epsilon\delta$ with $\epsilon \ll 1$, then the scaling is $E' = \epsilon^{3/2}E$, $\Omega' = \epsilon\Omega$ and the flow field is sought in the following

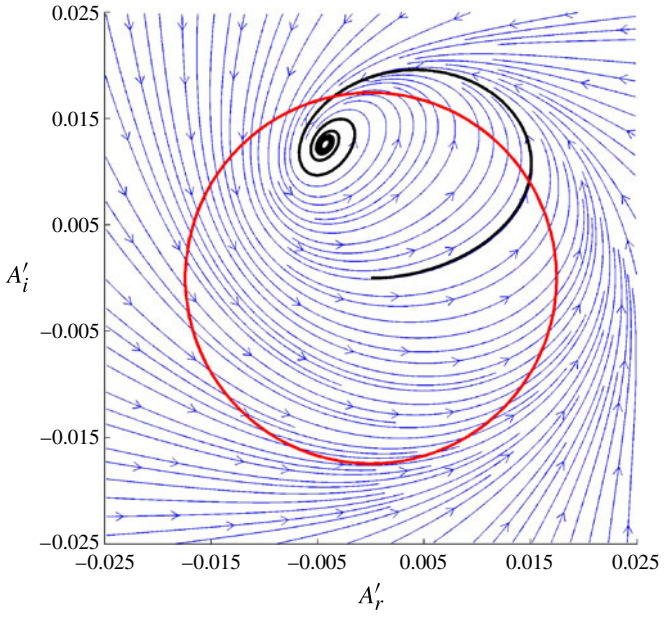

FIGURE 12. (Colour online) Phase portrait for supercritical Reynolds number $Re = 6250$ and forcing characterized by frequency $\omega_f = \omega_c = 7.0$ ($\Omega' = 0$) and amplitude $E' = 1.7 \times 10^{-5}$. The thick black line is a trajectory that starts at the origin. All trajectories converge towards a fixed point A_0'. The circle designates the limit cycle in the case of no control.

form:

$$\boldsymbol{q} = \boldsymbol{q}_0 + \epsilon^{1/2}[A\mathrm{e}^{\mathrm{i}\omega_c t}\boldsymbol{q}_A + \text{c.c.}] + \epsilon[\delta\boldsymbol{q}_\delta + |A|^2\boldsymbol{q}_{A\bar{A}} + (A^2\mathrm{e}^{2\mathrm{i}\omega_c t}\boldsymbol{q}_{AA} + \text{c.c.})]. \tag{4.1}$$

We introduce this development in the forced Navier–Stokes equation (3.2). The flow structures appearing in (4.1) are the same as those introduced in § 2. One may straightforwardly check that none of the linear systems involved here is degenerate. The equation governing the amplitude $A' = \epsilon^{1/2}\mathrm{e}^{-\mathrm{i}\epsilon\Omega t}A$ reads

$$\frac{\mathrm{d}A'}{\mathrm{d}t} = (\eta\delta' - \mathrm{i}\Omega')A' - \nu A'|A'|^2 + \mu E', \tag{4.2}$$

with $\mu = \langle\tilde{\boldsymbol{u}}_A, \boldsymbol{f}_E\rangle$. The structure of the amplitude equation is different from that obtained in the non-resonant case: the forcing term no longer changes the eigenvalue of the linear dynamics of the global mode but appears as an external constant forcing term. The magnitude of the coefficient μ is largest if we choose the adjoint global mode $\tilde{\boldsymbol{u}}_A$ as the forcing structure $\boldsymbol{f}_E$. If we normalize the forcing $\boldsymbol{f}_E$ to unit energy, $\boldsymbol{f}_E = \tilde{\boldsymbol{u}}_A/\|\tilde{\boldsymbol{u}}_A\|$, the coefficient μ is a positive real $\mu = 119.38$.

We now study the dynamics of the flow in the case $Re = 6250$. This is the supercritical configuration introduced in § 3.4: a single unstable global mode exists at this Reynolds number and the flow converges on a limit cycle in the uncontrolled case. A phase diagram of the dynamics is shown in figure 12. The circle depicts the limit cycle of amplitude $|A'| = 0.0174$. In the case of control, the dynamics converges towards a fixed point for sufficiently high forcing amplitudes E'. In the case of an exactly resonating forcing $\Omega' = 0$, the threshold value for this forcing amplitude to reach a fixed point is equal to $E_s' = 1.7 \times 10^{-5}$. The trajectories in the phase plane

corresponding to this threshold value are shown with black solid lines in figure 12. The fixed point A'_0 is located inside the limit cycle and close to it: the resulting flow therefore displays slightly lower-amplitude oscillations than the uncontrolled flow. Moreover, the frequency of the flow field is changed since the flow is no longer located on a limit cycle but on a fixed point. The resulting frequency of the flow is best analysed by rewriting the two dominant terms in expansion (4.1) in the form

$$\boldsymbol{q} = \boldsymbol{q}_0 + (A' \mathrm{e}^{\mathrm{i}(\omega_c + \Omega')t} \boldsymbol{q}_A + \text{c.c.}). \tag{4.3}$$

Hence, if the amplitude A' converges on a fixed point A'_0, then the frequency of the flow is seen to be $\omega_c + \Omega'$, which is simply the chosen forcing frequency ω_f. This is the well-known locking phenomenon as presented by Fauve (1998): if the forcing frequency ω_f is chosen close to the resonant frequency ω_c, then the flow locks onto the forcing frequency ω_f. Note that the required forcing amplitude $E' = \epsilon^{3/2} E$ is one order of magnitude lower than in the non-resonant case of § 3 where $E' = \epsilon^{1/2} E$. Near-resonance forcing is therefore an extremely cheap way to control the flow. If in an application it is sufficient to shift the frequency of the flow slightly, then this is certainly the best way to proceed. However, if we aim at suppressing the unsteadiness of the flow in a larger frequency band (as for example achieved in figure 9) then the best strategy is to apply a non-resonant forcing characterized by a frequency chosen at the local maxima displayed in figure 4.

Similarly to § 3.4, we have checked the validity of the weakly nonlinear analysis against DNS. We chose the same forcing as that analysed in figure 12: the forcing is characterized by the frequency $\omega_f = 7.0$, and the spatial structure by $\boldsymbol{f}_E = \tilde{\boldsymbol{u}}_A$. In figure 13(*a–d*), we have respectively represented (black lines) the cross-stream component of the flow field at point $(x = 0.75, y = 0)$ as a function of time for four different forcing amplitudes, $E' = 0.5E'_s$, E'_s, $2E'_s$, $4E'_s$, where $E'_s = 1.7 \times 10^{-5}$ is the threshold amplitude forcing to reach a fixed point. The control is switched on at $t = 92.2$: it is seen that in the uncontrolled case ($t < 92.2$), the DNS simulation displays oscillations whose amplitude approximately matches the one predicted by the amplitude equation (see the two horizontal lines on the left of the figures). Also, the red lines indicate the local frequency of the oscillations obtained in the DNS. They were obtained with the same algorithm as the one introduced in figure 8(*b*). It is seen that the natural frequency of the flow on the limit cycle is $\omega = 7.23$. In the case of control ($t > 92.2$), the behaviour of the flow depends on the forcing amplitude E'. For small-amplitude forcing $E' = 0.5E'_s$ (figure 13*a*), a low-frequency modulation of the signal $v(x = 0.75, y = 0, t)$ is observed: the amplitude of the oscillations increases and decreases periodically while the frequency oscillates around the natural frequency of the flow $\omega = 7.23$. At higher forcing amplitude $E' = E'_s$ (figure 13*b*), this behaviour is amplified. The amplitude and frequency oscillations strengthen but the locking phenomenon is not observed: the frequency still oscillates around the natural frequency of the flow. The asymptotic analysis therefore underestimates the amplitude threshold that achieves locking of the flow field. For twice the predicted amplitude threshold $E' = 2E'_s$ (figure 13*c*), we observe the locking phenomenon: the local frequency of the oscillations decreases down to the forcing frequency $\omega_f = 7.0$ and the amplitude of the oscillations converges towards a fixed value which is slightly smaller than the amplitude predicted by the asymptotic approach (see the two horizontal lines on the right of the figures). For an even higher forcing amplitude $E' = 4E'_s$ (figure 13*d*), a similar locking phenomenon is observed. However, we also observe differences: the amplitude of the oscillations again increases and decreases periodically and the

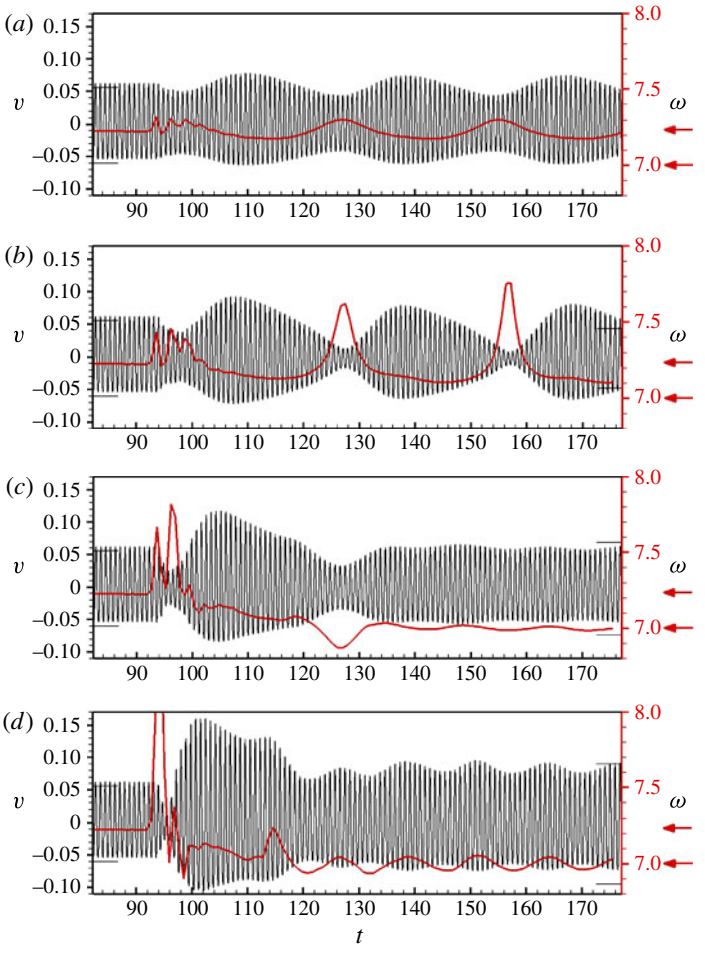

FIGURE 13. DNS at $Re = 6250$ with forcing switched on at $t = 92.2$ and characterized by $\omega_f = 7.0$ and $\boldsymbol{f}_E = \tilde{\boldsymbol{u}}_A$. The cross-stream velocity in the shear layer $v(x = 0.75, y = 0, t)$ is represented by a black line as a function of time (black y-axis). The local frequency is shown by the red line (red y-axis). For this, an algorithm tracks the occurrence in time of three consecutive extrema t_0, t_1 and t_2: t_0 is reported on the x-axis and $2\pi/(t_2 - t_0)$ on the y-axis. The arrows on the right of the plots show the natural frequency of the flow $\omega = 7.23$ and the forcing frequency $\omega_f = 7.0$. The forcing amplitude E' is different in each plot: (*a*) $E' = 0.5E'_s$; (*b*) $E' = E'_s$; (*c*) $E' = 2E'_s$; (*d*) $E' = 4E'_s$. Here $E'_s = 1.7 \times 10^{-5}$ is the threshold forcing amplitude that achieves locking of the frequency. The black horizontal lines on the left and on the right of the figures indicate the oscillation amplitudes predicted by the asymptotic analysis in the uncontrolled and controlled cases.

frequency of the signal now oscillates around the forcing frequency $\omega_f = 7.0$, which still ensures that the flow field is locked onto the forcing frequency.

4.2. *Forcing at* $\omega_f = 0$

For the sake of completeness, we briefly present the case of zero-frequency forcing ($\omega_f = 0$). This steady forcing case has already been treated by Marquet *et al.* (2008*a*) with a Lagrangian approach in the case of a cylinder flow. We show here how a

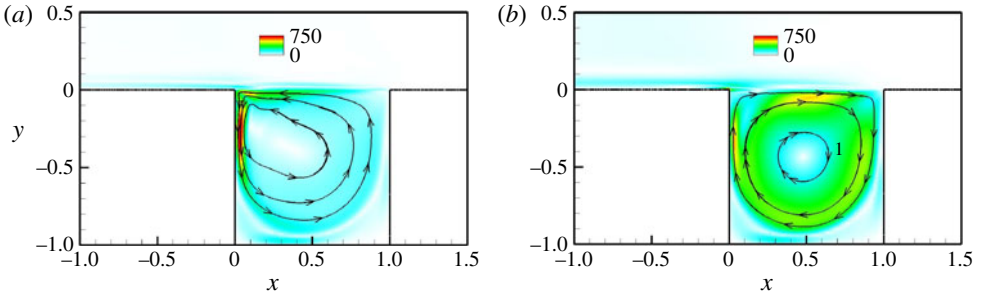

FIGURE 14. Case of steady forcing ($\omega_f = 0$). (a) Sensitivity of amplification rate to the introduction of a steady forcing $\nabla_f \sigma$. (b) Sensitivity of frequency to the introduction of a steady forcing $\nabla_f \omega$.

weakly nonlinear approach recovers the sensitivity maps introduced in Marquet *et al.* (2008*a*).

The scalings to be used in this case are $\delta' = \epsilon\delta$, $E' = \epsilon E$ (Marquet *et al.* 2008*b*). The flow field is sought in the form

$$\boldsymbol{q} = \boldsymbol{q}_0 + \epsilon^{1/2}[A\mathrm{e}^{\mathrm{i}\omega_c t}\boldsymbol{q}_A + \mathrm{c.c.}] + \epsilon[\delta\boldsymbol{q}_\delta + |A|^2\boldsymbol{q}_{A\bar{A}} + (A^2\mathrm{e}^{2\mathrm{i}\omega_c t}\boldsymbol{q}_{AA} + \mathrm{c.c.}) + E\boldsymbol{q}_E]. \quad (4.4)$$

The flow structures appearing in (4.4) are the same as those introduced in § 2. The new structure $\boldsymbol{q}_E$ appearing at order ϵ is governed by

$$\mathscr{M}\boldsymbol{q}_E = 2\mathscr{P}(\boldsymbol{f}_E). \quad (4.5)$$

It corresponds to the modification of the base flow due to the introduction of the steady forcing $\boldsymbol{f}_E$. The equation governing the amplitude $A' = \epsilon^{1/2}A$ reads

$$\frac{\mathrm{d}A'}{\mathrm{d}t} = (\eta\delta' + \mu E')A' - \nu A'|A'|^2. \quad (4.6)$$

It is seen that the steady forcing modifies the linear dynamics since the eigenvalue governing the dynamics of the global mode is $\lambda = \mathrm{i}\omega_c + \eta\delta' + \mu E'$. Hence, this situation is analogous to the non-resonant forcing case described in § 3.

The complex constant μ, which is obtained as before by imposing a compatibility condition at order $\epsilon^{3/2}$, is related to the modification of the base flow due to the steady forcing: $\mu = -\langle\tilde{\boldsymbol{u}}_A, \nabla\boldsymbol{u}_A\cdot\boldsymbol{u}_E + \nabla\boldsymbol{u}_E\cdot\boldsymbol{u}_A\rangle$. It is possible to relate this coefficient μ to the sensitivity maps introduced in Marquet *et al.* (2008*a*). For this, after performing some integration by parts, μ may be rewritten as $\mu = \langle\nabla_{\boldsymbol{u}_0}\lambda, \boldsymbol{u}_E\rangle = 2\langle\nabla_f\lambda, \boldsymbol{f}_E\rangle$, where $\nabla_{\boldsymbol{u}_0}\lambda = \nabla\tilde{\boldsymbol{u}}_A\cdot\overline{\boldsymbol{u}_A} - (\nabla\boldsymbol{u}_A)^*\cdot\tilde{\boldsymbol{u}}_A$ is the sensitivity of the eigenvalue λ with respect to a modification of the base flow $\boldsymbol{u}_0$, while $\nabla_f\lambda = \mathscr{P}^{\mathrm{T}}[\tilde{\mathscr{M}}^{-1}\mathscr{P}(\nabla_{\boldsymbol{u}_0}\lambda)]$ is the sensitivity of the eigenvalue to the introduction of a steady forcing (Marquet *et al.* 2008*a*). The sensitivity of the amplification rate ($\nabla_f\sigma = \mathrm{Re}(\nabla_f\lambda)$) and frequency ($\nabla_f\omega = -\mathrm{Im}(\nabla_f\lambda)$) to the introduction of a steady forcing are represented in figure 14(*a*,*b*). The solid lines with arrows indicate the orientation of the sensitivity fields while the coloured iso-contours refer to the norm of the fields. It is seen that the amplification rate of the global mode is most sensitive to the introduction of a steady forcing near the upstream wall of the cavity while the frequency is sensitive in a broad region inside the cavity. Also, a steady forcing that will accelerate the clockwise movement of the fluid inside the cavity is seen to increase the frequency and decrease

the amplification rate. This is in accordance with the fact that the velocity gradient in the shear layer (and therefore the Kelvin–Helmholtz instability mechanism) will be weaker and the downstream convection of the perturbations along the shear layer quicker.

5. Conclusion

This paper is concerned with open-loop control of oscillator flows with harmonic forcings. We have taken a particular oscillator flow, an open-cavity flow, to present the approach. This flow undergoes a supercritical Hopf bifurcation at $Re = 5396$. For supercritical Reynolds numbers, the flow is unstable and converges towards a limit cycle. This behaviour is well described by the Stuart–Landau equation (2.10), which governs the dynamics of the unstable global mode. We then considered the case of a harmonic forcing, which is characterized by a frequency ω_f, an amplitude E' and a spatial structure $\boldsymbol{f}_E$. More precisely, we look at how the forcing enters the amplitude equation (2.10). As in the case of a forced Van der Pol oscillator, the response of the flow depends on the forcing frequencies.

In the case where ω_f is not close to $0, \omega_c/2, \omega_c, 2\omega_c$, then the forcing modifies the linear dynamics of the global mode (see (3.9)). Due to nonlinear interactions, the zeroth harmonic $\boldsymbol{u}_{E\bar{E}}$, the $(\omega_c + \omega_f)$-harmonic $\boldsymbol{u}_{AE}$ and the $(\omega_c - \omega_f)$-harmonic $\boldsymbol{u}_{A\bar{E}}$ yield an additional term $-\mu(\omega_f)E'^2A'$ in the amplitude equation. Two control strategies were then presented. First, the stabilizing strategy, only possible at frequencies where $\mu_r(\omega_f) > 0$, consists in stabilizing the global mode. If the forcing frequency is higher than ω_c, this leads to the suppression of all perturbations whose frequencies are lower than the forcing frequency. Second, shifting the frequency of the flow on the limit cycle aims at changing the frequency of the flow field. A complete study over all frequencies has been achieved, showing where the forcing stabilizes the flow, where the forcing increases or decreases the frequency of the flow. Also, we have shown that there are particular frequencies where the forcing amplitude is lowest to achieve a strongest impact on the flow. These frequencies correspond to local extrema of $|\mu_r(\omega_f)|$ and $|\gamma(\omega_f)|$ (see (3.16)). The spatial structure $\boldsymbol{f}_E$ of the forcing may also be optimized to diminish the forcing amplitude E'. For this, we considered optimal forcings, which at a given frequency yield the strongest energy response. These optimal forcings depend on the forcing frequency ω_f and may be obtained by finding the strongest singular values of the resolvent matrix. These structures are located on the shear layer, close to the leading edge of the cavity. Comparing the response of a flow triggered by optimal forcings with the case of a flow manipulated by a fixed localized forcing situated near the leading edge of the cavity, we showed that the forcing amplitude E' may be decreased by an order of magnitude with the optimal forcings. For the stabilization strategy, we confirmed the validity of the developments by performing direct numerical simulation at the supercritical Reynolds number $Re = 6250$. The behaviour predicted by the amplitude equation is nicely recovered by the DNS: after a short transient period, the spectrum of the flow only displays peaks near the forcing frequency and its harmonics, while the peaks associated to the global mode have completely disappeared. Finally, the stability properties of the resulting mean flows were analysed. In the presence of control, it was shown that, if the zeroth harmonic $\boldsymbol{u}_{E\bar{E}}$ dominates the $(\omega_c + \omega_f)$-harmonic $\boldsymbol{u}_{AE}$ and the $(\omega_c - \omega_f)$-harmonic $\boldsymbol{u}_{A\bar{E}}$, then the linear dynamics of the global mode is governed by the eigenvalue resulting from a stability analysis based on the mean flow (and not on the base flow). The same condition ensures that the mean flow resulting from a stabilization strategy is marginally stable and that the mean flow resulting from a 'frequency shifting strategy' displays the frequency of the true manipulated flow field.

In the case where the forcing frequency is close to the natural frequency of the flow $\omega_f \approx \omega_c$, then the forcing enters the amplitude equation as an external constant forcing term $\mu E'$. The coefficient μ is strongest if the forcing structure $\boldsymbol{f}_E$ is chosen to be the adjoint global mode $\tilde{\boldsymbol{u}}_A$. The study of the amplitude equation shows that the flow locks onto the forcing frequency for a sufficiently high forcing amplitude E'. The scalings used here show that the forcing amplitude E' is an order of magnitude lower than in the non-resonant case. Therefore, a near-resonant forcing is certainly the cheapest strategy to slightly change the frequency of an oscillator. Finally, the predictions of the amplitude equation were checked against a forced direct numerical simulation conducted at the supercritical Reynolds number $Re = 6250$, where the locking phenomenon occurred at approximately twice the forcing amplitude E'_s predicted by theory.

For the sake of completeness, we also treated the case of steady forcing. Similarly to the non-resonant case, the forcing modifies the linear dynamics of the global mode by adding a term $\mu E'A'$ to the amplitude equation (see (4.6)). In particular, we showed how the sensitivity fields introduced by Marquet *et al.* (2008*a*) may be retrieved from the coefficient μ.

For future work, we plan to extend the present study in three directions. First, we would like to treat the case of steady three-dimensional forcing. Indeed, Kim & Choi (2005) have nicely shown how a steady three-dimensional blowing and suction applied along the span of a cylinder managed to decrease its drag strongly. According to Choi *et al.* (2008), such a forcing directly acts on the wake and not on the mean boundary layer separation position. In particular, it will be interesting to study the induced mean flow as a function of the transverse wavelength of the blowing/suction profile. Second, nearly all studies with synthetic jets (Glezer & Amitay 2002) concern turbulent flows. Usually, the forcing frequency is an order of magnitude higher than the natural frequency of the flow, to ensure that the behaviour of the flow field (and in particular the drag and lift coefficients) do not depend on the forcing frequency. It would be interesting to question these hypotheses using the present systematic approach based on a weakly nonlinear approach. For this, we could use unsteady Reynolds-averaged Navier–Stokes equations with a turbulence model such as the $k-\omega$ turbulence model. In the case of a transonic, high Reynolds number flow over an open cavity, we know that such a model is quite accurate in capturing the Rossiter flow oscillations. Third, it would be interesting to extend the present approach to amplifier flows, such as jets or boundary layer flows. For example, Wiltse & Glezer (1998) studied the manipulation of a jet using synthetic jets. A systematic theoretical approach describing the effect of the chosen forcing frequency with respect to the natural broadband frequencies of the flow would be helpful in understanding the physical mechanisms at play in such open-loop control studies.

Acknowledgement

The author would like to thank O. Marquet for fruitful discussions.

Supplementary movie

A supplementary movie is available at http://dx.doi.org/10.1017.jfm.2012.329.

Appendix A. Blowing and suction

The case of blowing and suction may be treated in a straightforward way. The governing equations are given by the original unforced Navier–Stokes equations (2.1)

and the forced solution is still sought in the form (3.3). At order $\epsilon^{1/2}$, instead of (3.4), we use the following equation to determine $\boldsymbol{q}_E$:

$$(\mathrm{i}\omega_f \mathscr{P}\mathscr{P}^{\mathrm{T}} + \mathscr{M})\boldsymbol{q}_E = \boldsymbol{0}, \tag{A 1}$$

with $\mathscr{P}^{\mathrm{T}}\boldsymbol{q}_E = \boldsymbol{u}_C$ on some given forcing boundary Γ_C. Here $\boldsymbol{u}_C$ is a given blowing/suction profile defined on Γ_C. Once $\boldsymbol{q}_E$ is computed, the rest of the analysis holds.

Appendix B. Forcing near $\omega_f = 2\omega_c$

We choose a forcing frequency ω_f close to $2\omega_c$: $\omega_f = 2\omega_c + \Omega'$. The scaling is $E' = \epsilon E$ and $\Omega' = \epsilon\Omega$ and the solution is sought in the form

$$\begin{aligned}\boldsymbol{q} = \boldsymbol{q}_0 &+ \epsilon^{1/2}[A\mathrm{e}^{\mathrm{i}\omega_c t}\boldsymbol{q}_A + \text{c.c.}] \\ &+ \epsilon[\delta\boldsymbol{q}_\delta + |A|^2\boldsymbol{q}_{A\bar{A}} + (A^2\mathrm{e}^{2\mathrm{i}\omega_c t}\boldsymbol{q}_{AA} + \text{c.c.}) + (E\mathrm{e}^{2\mathrm{i}\omega_c t}\boldsymbol{q}_E + \text{c.c.})].\end{aligned} \tag{B 1}$$

The forcing response may be obtained via

$$(2\mathrm{i}\omega_c \mathscr{P}\mathscr{P}^{\mathrm{T}} + \mathscr{M})\boldsymbol{q}_E = \mathscr{P}(\boldsymbol{f}_E). \tag{B 2}$$

The equation governing the amplitude $A' = \epsilon^{1/2}\mathrm{e}^{-\mathrm{i}\epsilon\Omega t/2}A$ reads

$$\frac{\mathrm{d}A'}{\mathrm{d}t} = (\eta\delta' - \mathrm{i}\Omega'/2)A' - \nu A'|A'|^2 + \mu E'\bar{A}', \tag{B 3}$$

where μ is a complex constant resulting from the nonlinear interaction of the conjugate of the global mode with the forcing response $\boldsymbol{q}_E$:

$$\mu = -\langle \tilde{\boldsymbol{u}}_A, \overline{\boldsymbol{\nabla}\boldsymbol{u}_A}\cdot\boldsymbol{u}_E + \boldsymbol{\nabla}\boldsymbol{u}_E\cdot\overline{\boldsymbol{u}_A}\rangle. \tag{B 4}$$

For the supercritical Reynolds number $Re = 6250$, we show in figure 15(*a*) the phase plane associated to the amplitude equation (B 3). We use the optimal forcing at frequency $2\omega_c$ as the forcing structure $\boldsymbol{f}_E$. In this case, μ is complex and equal to $\mu = -372.7 + 79.55\mathrm{i}$. The threshold value to obtain a fixed point is $E' = 4.01 \times 10^{-4}$. The fixed point is located inside the circle, which shows that the resulting flow exhibits slightly weaker oscillation amplitudes than the uncontrolled flow. The frequency of the flow is obtained by rewriting the dominant terms in the expansion (B 1) as

$$\boldsymbol{q} = \boldsymbol{q}_0 + (A'\mathrm{e}^{\mathrm{i}(\omega_c + \Omega'/2)t}\boldsymbol{q}_A + \text{c.c.}). \tag{B 5}$$

Hence, the frequency of the unsteadiness in the flow is $\omega_c + \Omega'/2$.

Appendix C. Forcing near $\omega_f = \omega_c/2$

We choose a forcing frequency ω_f close to $\omega_c/2$: $\omega_f = \omega_c/2 + \Omega'$. The scaling is $E' = \epsilon^{3/4}E$ and $\Omega' = \epsilon\Omega$ while the solution is sought in the form

$$\begin{aligned}\boldsymbol{q} = \boldsymbol{q}_0 &+ \epsilon^{1/2}[A\mathrm{e}^{\mathrm{i}\omega_c t}\boldsymbol{q}_A + \text{c.c.}] \\ &+ \epsilon^{3/4}[(E\mathrm{e}^{\mathrm{i}(\omega_c/2)t}\boldsymbol{q}_E + \text{c.c.})] + \epsilon[\delta\boldsymbol{q}_\delta + |A|^2\boldsymbol{q}_{A\bar{A}} + (A^2\mathrm{e}^{2\mathrm{i}\omega_c t}\boldsymbol{q}_{AA} + \text{c.c.})].\end{aligned} \tag{C 1}$$

The forcing response may be obtained via

$$(\mathrm{i}(\omega_c/2)\mathscr{P}\mathscr{P}^{\mathrm{T}} + \mathscr{M})\boldsymbol{q}_E = \mathscr{P}(\boldsymbol{f}_E). \tag{C 2}$$

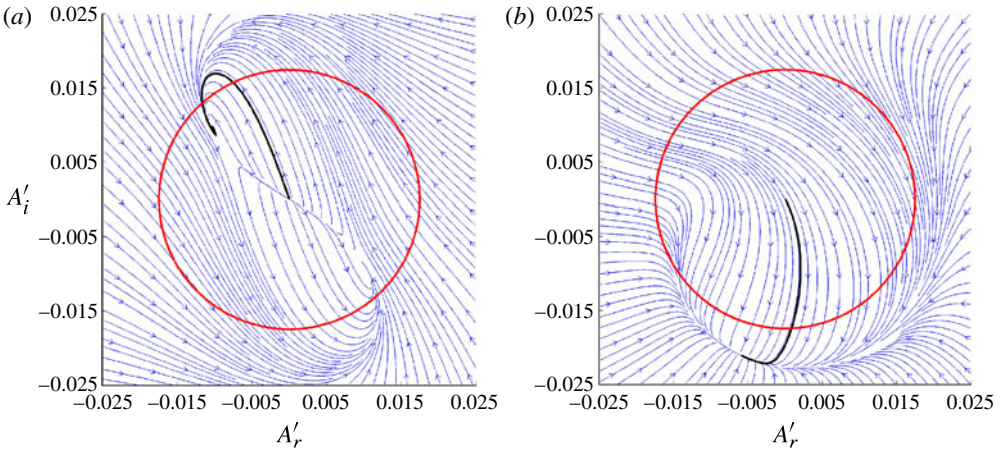

FIGURE 15. (Colour online) (*a*) Phase portrait in resonant case $\omega_f = 2\omega_c$ ($\Omega' = 0$) for forcing amplitude $E' = 4.01 \times 10^{-4}$. (*b*) Resonant case $\omega_f = \omega_c/2$ ($\Omega' = 0$) for forcing amplitude $E' = 8.4 \times 10^{-4}$. The thick black line in each plot is a trajectory that starts near the origin. All trajectories converge towards a fixed point. The circle designates the limit cycle in the case of no control.

The equation governing the amplitude $A' = \epsilon^{1/2} \mathrm{e}^{-2\mathrm{i}\epsilon\Omega t} A$ reads

$$\frac{\mathrm{d}A'}{\mathrm{d}t} = (\eta\delta' - 2\mathrm{i}\Omega')A - \nu A'|A'|^2 + \mu E'^2, \tag{C 3}$$

where μ is a complex constant resulting from the nonlinear interaction of the forcing amplitude with itself: $\mu = -\langle \tilde{\boldsymbol{u}}_A, \boldsymbol{\nabla} \boldsymbol{u}_E \cdot \boldsymbol{u}_E \rangle$. As in the case of a forcing frequency close to the natural frequency of the flow, the forcing enters the amplitude equation as an external constant forcing term. For the supercritical Reynolds number $Re = 6250$, we show in figure 15(*b*) the phase plane associated to the amplitude equation (C 3). We use the optimal forcing at frequency $\omega_c/2$ for the forcing structure $\boldsymbol{f}_E$. In this case, μ is complex and equal to $\mu = 1314 - 2578\mathrm{i}$. The threshold value to obtain a fixed point is $E' = 8.4 \times 10^{-4}$. The fixed point is this time located outside the circle, which shows that the resulting flow exhibits slightly stronger oscillation amplitudes than the uncontrolled flow. The frequency of the flow is obtained by rewriting the dominant terms in the expansion (C 1) as

$$\boldsymbol{q} = \boldsymbol{q}_0 + (A' \mathrm{e}^{\mathrm{i}(\omega_c + 2\Omega')t} \boldsymbol{q}_A + \text{c.c.}). \tag{C 4}$$

Hence, the frequency of the unsteadiness in the flow is $\omega_c + 2\Omega'$. The frequency shift is larger than in § 4.1 and appendix B. However, the forcing amplitude here ($E' = \epsilon^{3/4} E$) is also required to be higher than there ($E' = \epsilon^{3/2} E$ and $E' = \epsilon E$).

REFERENCES

ALIZARD, F. & ROBINET, J.-C. 2007 Spatially convective global modes in a boundary layer. *Phys. Fluids* **19** (11), 114105.

AMESTOY, P. R., DUFF, I. S., KOSTER, J. & L'EXCELLENT, J.-Y. 2001 A fully asynchronous multifrontal solver using distributed dynamic scheduling. *SIAM J. Math. Anal. Appl.* **23** (1), 15–41.

AMITAY, M., SMITH, D. R., KIBENS, V., PAREKH, D. E. & GLEZER, A. 1998 Aerodynamic flow control over an unconventional airfoil using synthetic jet actuators. *AIAA J.* **39**, 361–370.

BARBAGALLO, A., SIPP, D. & SCHMID, P. J. 2009 Closed-loop control of an open cavity flow using reduced-order models. *J. Fluid. Mech.* **641**, 1–50.

BARKLEY, D. 2006 Linear analysis of the cylinder wake mean flow. *Europhys. Lett.* **75** (5), 750–756.

BENDER, C. M. & ORSZAG, S. A. 1978 *Advanced Mathematical Methods for Scientists and Engineers: Asymptotic Methods and Perturbation Theory*. McGraw-Hill.

BRANDT, L., SIPP, D., PRALITS, J. & MARQUET, O. 2011 Effect of base-flow variation in noise amplifiers: the flat-plate boundary layer. *J. Fluid Mech.* **687**, 503–528.

CHOI, H., JEON, W.-P. & KIM, J. 2008 Control of flow over a bluff body. *Annu. Rev. Fluid Mech.* **40**, 113–139.

CHOMAZ, J.-M. 2005 Global instabilities in spatially developing flows: non-normality and nonlinearity. *Annu. Rev. Fluid Mech.* **37**, 357–392.

FAUVE, S. 1998 Pattern forming instabilities. In *Hydrodynamics and Nonlinear Instabilities* (ed. C. Godrèche & P. Manneville), pp. 387–492. Cambridge University Press.

GIANNETTI, F., CAMARRI, S. & LUCHINI, P. 2010 Structural sensitivity of the secondary instability in the wake of a circular cylinder. *J. Fluid Mech.* **651**, 319–337.

GIANNETTI, F. & LUCHINI, P. 2007 Structural sensitivity of the first instability of the cylinder wake. *J. Fluid Mech.* **581**, 167–197.

GLEZER, A. & AMITAY, M. 2002 Synthetic jets. *Annu. Rev. Fluid Mech.* **24**, 503–529.

GLOWINSKI, R. 2003 Finite element methods for incompressible viscous flow. In *Handbook of Numerical Analysis* (ed. P. G. Ciarlet & J. L. Lions), vol. IX. pp. 3–1176. North-Holland.

HILL, D. C. 1992 A theoretical approach for analysing the restabilization of wakes. *AIAA paper* 1992-0067.

HUERRE, P & ROSSI, M. 1998 Hydrodynamic instabilities in open flows. In *Hydrodynamics and Nonlinear Instabilities* (ed. C. Godrèche & P. Manneville), pp. 81–294. Cambridge University Press.

HWANG, Y. & CHOI, H. 2006 Control of absolute instability by basic-flow modification in a parallel wake at low Reynolds number. *J. Fluid Mech.* **560**, 465–475.

ILLY, H., GEFFROY, P. & JACQUIN, L. 2008, Observations on the passive control of flow oscillations over a cavity in a transonic regime by means of a spanwise cylinder. *AIAA paper* 2008-3774.

JACKSON, C. P. 1987 A finite-element study of the onset of vortex shedding in flow past variously shaped bodies. *J. Fluid Mech.* **182**, 23–45.

KEIRSBULCK, L., EL HASSAN, M., LIPPERT, M. & LABRAGA, L. 2008 Control of cavity tones using a spanwise cylinder. *Can. J. Phys.* **86** (12), 1355–1365.

KIM, J. & CHOI, H. 2005 Distributed forcing of flow over a circular cylinder. *Phys. Fluids* **17**, 033103.

LEHOUCQ, R. B. & SORENSEN, D. C. 1996 Deflation techniques for an implicitly restarted Arnoldi iteration. *SIAM J. Math. Anal. Appl.* **17** (4), 789–821.

MARQUET, O., SIPP, D., CHOMAZ, J.-M. & JACQUIN, L. 2008*a* Amplifier and resonator dynamics of a low-Reynolds-number recirculation bubble in a global framework. *J. Fluid Mech.* **605**, 429–443.

MARQUET, O., SIPP, D., JACQUIN, L. & CHOMAZ, J.-M. 2008*b* Multiple time scale analysis and sensitivity analysis for the passive control of the cylinder flow. In *5th AIAA Theoretical Fluid Mechanics Conference, 23–26 June 2008, Seattle, Washington. AIAA paper* 2008-4228.

MELIGA, P. & CHOMAZ, J.-M. 2011 An asymptotic expansion for the vortex-induced vibrations of a circular cylinder. *J. Fluid Mech.* **671**, 137–167.

MELIGA, P., CHOMAZ, J.-M. & SIPP, D. 2009 Global mode interaction and pattern selection in the wake of a disk: a weakly nonlinear expansion. *J. Fluid Mech.* **633**, 159–189.

MELIGA, P., SIPP, D. & CHOMAZ, J. -M. 2010 Open-loop control of compressible afterbody flows using adjoint methods. *Phys. Fluids* **22**, 054109.

MONOKROUSOS, A., AKERVIK, E., BRANDT, L. & HENNINGSON, D. S. 2010 Global three-dimensional optimal disturbances in the Blasius boundary-layer flow using time-steppers. *J. Fluid Mech.* **650**, 181–214.

PIER, B 2003 Open-loop control of absolutely unstable domains. *Proc. R. Soc. Lond.* A **459**, 1105–1115.

PROVANSAL, M., MATHIS, C. & BOYER, L. 1987 Bénard–von Kármán instability: transient and forced regimes. *J. Fluid Mech.* **182**, 1–22.

ROSSITER, J. E. 1962 The effect of cavities on the buffeting of aircraft. *Royal Aircraft Establishment Tech. Mem.* **754**.

SIPP, D. & LEBEDEV, A. 2007 Global stability of base and mean flows: a general approach and its applications to cylinder and open cavity flows. *J. Fluid Mech.* **593**, 333–358.

SIPP, D. & MARQUET, O. 2012 Characterization of noise amplifiers with global singular modes: the case of the leading-edge flat-plate boundary layer. *Theor. Comput. Fluid. Dyn.* doi:10.1007/s00162-012-0265-y.

SIPP, D., MARQUET, O., MELIGA, O. & BARBAGALLO, A. 2010 Dynamics and control of global instabilities in open flows: a linearized approach. *Appl. Mech. Rev.* **63**, 030801.

STANEK, M. J., VISBAL, M. R., RIZZETTA, D. P., RUBIN, S. G. & KHOSLA, P. K. 2007 On a mechanism of stabilizing turbulent free shear layers in cavity flows. *Comput. Fluids* **36**, 1621–1637.

STRYKOWSKI, P. J. & SREENIVASAN, K. R. 1990 On the formation and suppression of vortex shedding at low Reynolds numbers. *J. Fluid Mech.* **218**, 71–107.

WILTSE, J. M. & GLEZER, A. 1998 Direct excitation of small-scale motions in free shear flows. *Phys. Fluids* **10** (8), 2026–2036.